Red Pigmentation of Mussel Shells at the Middle Grant Creek Site

Laura Richter
ANTH 42355 Lab Research Project
Professor Mark Schurr
Fall 2019

Introduction:

The Middle Grant Creek site is located in Northeastern Illinois, dating to the early seventeenth century.[1] It falls within the so-called Huber phase of the Oneota tradition, a prehistoric-protohistoric culture extending from Lake Michigan to the Missouri river.[2] Archaeological work at the site uncovered several mussel shells with fragments of red coloration on their exterior surfaces, appearing to be an applied pigment. This study utilizes several scientific analytical methods to examine the composition of these red portions, specifically interested in determining whether this color resulted from interactions with the surrounding soil following burial on site, or if it had been intentionally added.

Although mussels were used primarily as a food source within Oneota society, there is evidence that their shells were used, not only functionally as tools or as temper for pottery, but also for their appearance. For example, the elephant-ear and similarly striking shell varieties were buried with the dead.[3] Similarly, marine shells were often found within burials, worked into goods such as beads or ear plugs.[4] These examples demonstrate a possible interest in the shells within ritual contexts as ornamentation, manifesting possible motivation for adding coloration to their surfaces.

Mussel shells showing evidence of red pigmentation were found within subterranean storage pits, which were originally used to store maize, but eventually filled with refuse including ceramic, faunal and lithic debris.[5] Within Oneota sites as a whole, most mussels were

[1] McLeester et al., "Protohistoric Marine Shell Working," 550.
[2] Pauketat, *The Oxford Handbook of North American Archaeology*, 414.
[3] Theler and Boszhardt, *Twelve Millennia*, 209.
[4] McLeester et al., "Protohistoric Marine Shell Working," 549–50.
[5] McLeester et al., 550.

sourced from nearby bodies of water.[6] The majority of shells at Middle Grant Creek were most likely originally drawn from the nearby Kankakee River.

A variety of sites of the Oneota Culture demonstrate extensive use of hematite, a naturally occurring iron (III) oxide, for painting wall designs and a variety of objects, most often pottery.[7] Red ochre or paintstone were also used as pigment, although less frequently.[8] As a result, it was hypothesized that hematite ore could have been similarly ground and applied these shells.

Figure 1: The three mussel shells analyzed, labele d (from left to right), shell A, B, and C.

Procedure:

This study examined three shells from Middle Grant Creek. Two display red surface coloration as potentially added pigment, named shells A and B for the purposes of this study. The third, shell C, is a modern rather than archaeological shell, displaying red splotches on the interior, likely deposited through natural processes and included for comparison (see Fig. 1). Finally, soil samples from three levels of the pit, 8, 9 and 13 were analyzed. The greatest focus was placed on level 13 as adjacent to the location of the buried shells of this study, and the others

[6] Theler and Boszhardt, *Twelve Millennia*, 209.
[7] Berry and Chapman, "An Oneota Site in Missouri 1," 299.
[8] Chapman and Chapman, *Indians and Archaeology of Missouri, Revised Edition,* 73.

were included for comparison. Three primary scientific techniques were used to study the shell composition, detailed below.

X-ray fluorescence (XRF) is beneficial as a non-destructive technique allowing for fast and easy identification of elements contained within a sample.[9] However, the elemental acquisition of XRF is limited, most consistently identifying elements in the titanium through niobium range. Elements with low atomic numbers or with very low concentration within the sample generally cannot be detected utilizing this technique.[10] XRF analysis was used as a first method to compare red and plain white portions of shells A and B, alongside examining soil samples from the same storage pit. Both plain white portions of the shell from its exterior and interior were analyzed.

Additionally, a portion of shell B was analyzed using XRF mapping (Fig. 2), a process in which hundreds of points across a selected region, in this case approximately a centimeter, are analyzed and compiled to produce an image displaying the distribution of an individual element across the surface. In this case, images were produced to display the elementa distribution of Aluminum, Calcium, Iron, Potassium, Manganese, Silicon, and Titanium, all of which had appeared in single point analysis of the shell.

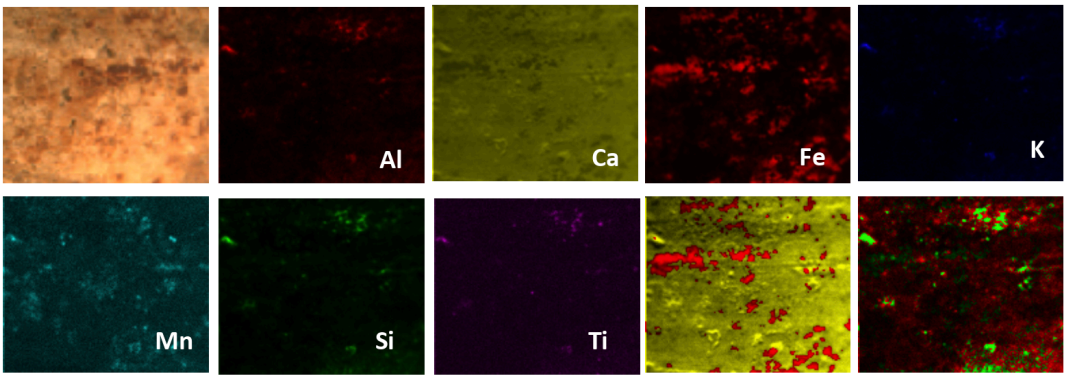

Figure 2: X-ray fluorescence mapping of Shell B

[9] Shackley, *X-Ray Fluorescence Spectrometry (XRF) in Geoarchaeology*, 8–9.
[10] Shackley, 10.

Information on the molecular composition of the shells and soil samples were acquired using Raman spectroscopy. Within this method, the Raman device bombards the sample with a laser beam of known wavelength. After hitting the sample, the scattered light reveals subtle energy variations due to changes in the vibrational states of the molecules making up the sample. The resulting Raman bands reflect the consequent difference between the incident radiation and scattered radiation. As a result, measuring this value reveals the energy of molecular vibrations, which in turn is determined through the atoms making up the molecule, the chemical bonds connecting them, and the physicochemical environment surrounding them.[11] Since the combination of bands and their relative intensities are unique to each molecular structure, comparing the resulting band with standard samples allows for identification of an unknown sample.

Raman spectroscopy as an analytical technique has several key advantages. It allows for in-situ study of the piece, without the need for removing an individual sample, is non-destructive, and has high special resolution. Additionally, a wide range of Raman data from a variety of archaeological artifacts allows for a wealth of comparative materials for identification and comparison of specific pigments. As a result, some scholars consider it to be the best analytical method for studying the pigmentation of archaeological artifacts.[12]

One major limitation to Raman spectroscopy, however, is fluorescence, especially challenging on an uneven and porous surface such as mussel shells. Fluorescence can be decreased using a lower power laser.[13] However, in this study a green laser of 532 nm was used for all final analysis. Although data collection was also taken using a red laser of lower energy,

[11] Creagh and Bradley, *Radiation in Art and Archeometry*, 81.
[12] Creagh and Bradley, 98.
[13] Creagh and Bradley, 98.

no improvement on peak size was observed. Instead, increasing the accumulations did demonstrate an observable decrease in fluorescence. Each of the final spectra included in Appendix B result from 20 accumulations of 20 seconds, for a total exposure time of 400 seconds.

The white surface was analyzed to determine specific shell composition, along with extensive studies of the red portions of shells A and B. These were compared both with the red portions from the interior of shell C and with the soil sample (level 13).

The final methodology used in this study, scanning electron microscopy (SEM), produces high-magnification images and elemental composition analysis of a sample. A beam of electrons, accelerated and focused on the sample, is scanned across the surface, providing a detailed picture of its surface morphology. The high depth of field additionally allows for the analysis of several layers of uneven surfaces.[14] Additionally, measuring the X-rays emitted from the specimen when under bombardment of the energetic electrons gives a picture of the elemental composition across its surface.[15]

Results:

The XRF map of the shell surface reveled that the red portions corresponded with areas of higher iron content (Fig. 2). Additionally, the concentrations of aluminum and silicon appeared to align with several small concentrated specks likely resulting from the aluminum silicates of the soil. Individual point analysis confirmed iron as the primary source of red coloration on the surface of the shell (Fig. 3). The plain white shell surface had minimal iron content, while a strong iron peak appeared on analysis of red colored portions. The calcium

[14] Frahm, "Scanning Electron Microscopy (SEM)," 755.
[15] Frahm, 755.

content from the shell, composed of calcium carbonate, remained high within regions of red pigmentation, but dropped significantly within brown, dirty regions, indicating that the red pigment had seeped into the shell surface, while the dirt retained a separate layer on its surface.

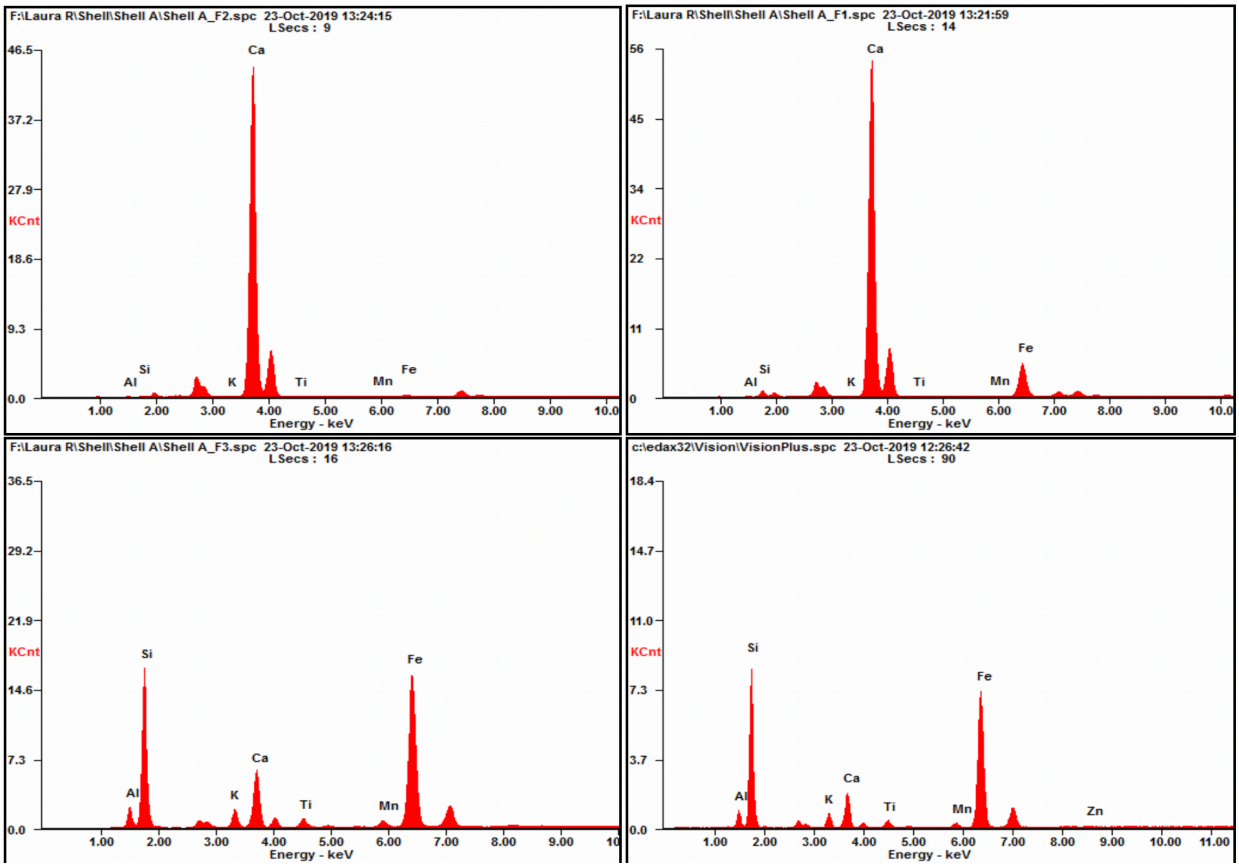

Figure 3: XRF graphs from shell B, from top left to bottom right, of the white, red, dirty portions of the shell, as well as a dirt sample (level 13). Figure 2: XRF graphs from shell B, from top left to bottom right, of the white, red, dirty portions of the shell, as well as a soil sample (level 13). See Appendix A for additional points and details.

The percent iron was higher both within dirty fragments on the shell and within the dirt sample (Fig. 3) with 9.22% and 9.17% iron by weight respectively compared to 7.19% within the red layer of the shell. As a result, the soil was not ruled out as a potential source for the iron coating the shell at this stage of analysis. However, the red pigmentation only appears on the exterior and XRF analysis of the interior surface of the shell confirmed minimal iron content, even in discolored

segments (see Appendix A). Likely, if iron were seeping from the soil onto the shell, it would be observed across both surfaces.

Raman analysis allowed for a distinction between the iron in the soil and within the red coloration of the shell. The soil sample had its highest intensity peak around 16000 cm^{-1}, which can be attributed to a C=C aromatic carbon double bond. Although carbon content in soil is not high, this peak is characteristic of soils because of its strong Raman scattering.[16] This peak additionally appeared at a much lower intensity on the shell surface. The soil also revealed several iron-containing molecules, specifically hematite, Fe_2O_3, and pyrite, FeS_2 (see Fig. 4).[17-18]

The largest peak of white portions of the shell appeared around 1080 cm^{-1}, which along with the peak at 710 cm^{-1}, can be attributed to calcite, the calcium carbonate making up the shell.[19] Along with a small peak from the soil, traces of a goethite peak at 390 cm^{-1} were observed.[20] This goethite (FeOOH) peak increased in intensity within Raman analysis of red colored portions of the shell (Fig. 4). As a result, though both the soil and red pigmentation of the shell demonstrated iron content as seen within XRF analysis, Raman data demonstrated that the molecular forms of that iron varied.

[16] Luna et al., "Classification of Soil Samples Based on Raman Spectroscopy and X-Ray Fluorescence Spectrometry Combined with Chemometric Methods and Variable Selection."
[17] "Hematite R070240 - RRUFF Database: Raman, X-Ray, Infrared, and Chemistry."
[18] "Pyrite R100166 - RRUFF Database: Raman, X-Ray, Infrared, and Chemistry."
[19] Marucci et al., "Raman Spectroscopic Library of Medieval Pigments Collected with Five Different Wavelengths for Investigation of Illuminated Manuscripts," 1223.
[20] Bellot-Gurlet et al., "Raman Studies of Corrosion Layers Formed on Archaeological Irons in Various Media," 150.

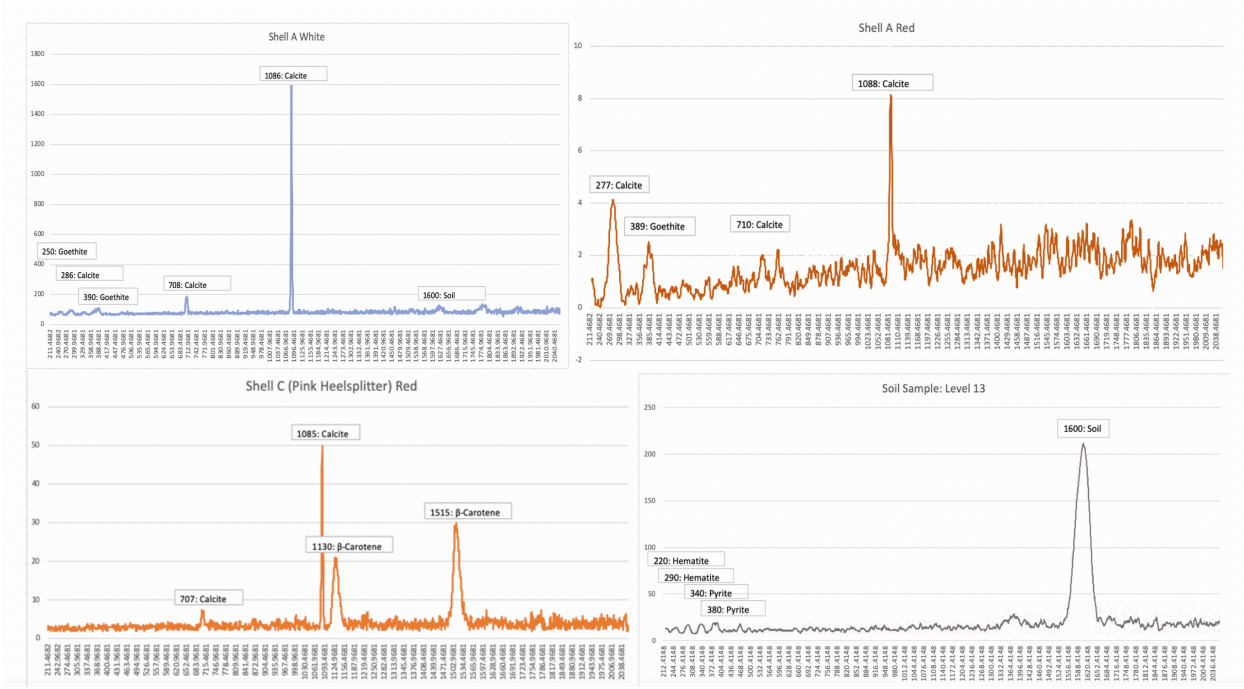

Figure 4: Raman spectra demonstrating three distinct sources of iron: goethite (iron oxyhydroxide, FeOOH), hematite (iron oxide, Fe_2O_3), pyrite (iron disulfide, FeS_2). Additionally, shell C demonstrated a non-iron source of red coloration, β-Carotene ($C_{40}H_{56}$). Additional Raman spectra included in Appendix B.

Finally, the red splotches inside shell C, the modern pink heelsplitter mussel shell were analyzed for comparison, as a natural surface red color similar in appearance. Raman spectroscopy confirmed that this red coloration was different in form from that on the archaeological samples. In this case, the red portions contained β-Carotene ($C_{40}H_{56}$).

The elemental composition observed through scanning electron microscopy (SEM) was drawn from an extremely small sample, allowing analysis to concentrate even more closely on red portions of the shell. As a result, a much larger percentage of iron than revealed through XRF analysis (see Fig 5). Additionally, the high oxygen content observed in SEM compositional analysis corresponds with the presence of iron oxyhydroxide, goethite, as an oxygen containing molecule.

Shell 1

Element	At. No.	Netto	Mass [%]	Mass Norm. [%]	Atom [%]	abs. error [%] (1 sigma)	rel. error [%] (1 sigma)
Oxygen	8	85397	21.57	31.07	49.81	2.48	11.48
Iron	26	84475	36.46	52.52	24.12	1.10	3.01
Carbon	6	9643	6.36	9.16	19.55	0.92	14.47
Silicon	14	40501	4.86	7.00	6.39	0.23	4.72
Titanium	22	768	0.17	0.24	0.13	0.03	19.78
		Sum	**69.43**	**100.00**	**100.00**		

Figure 5: SEM elemental composition analysis from red portion of Shell A

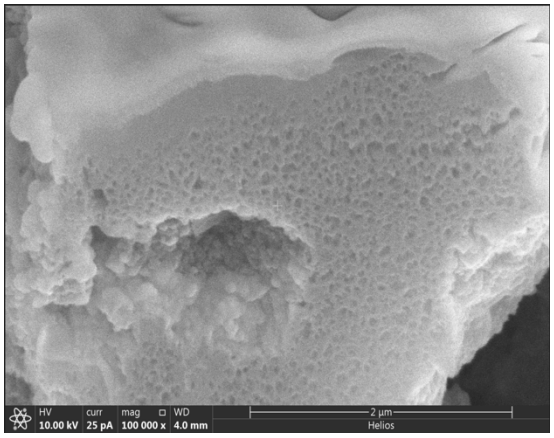

Figure 6: SEM image of shell cross-section

SEM additionally provided detailed images demonstrating the interaction between the layer of red pigmentation with the shell material. Specifically, in an approximately 4 µm cross-section of the colored shell surface, a smooth homogenous layer is observed laying on top of but also seeping into the porous shell (Fig. 6).

Images highlighting the concentrations of calcium, found in the calcium carbonate of the shell, and iron demonstrate a similar interaction between pigmentation and shell material. These SEM pictures demonstrate a distinct raised layer high in iron content on the surface of the shell. However, regions of iron and calcium are not entirely distinct. Iron-rich regions still show evidence of calcium, indicating that the red pigment seeped into the shell surface, exposing some calcium carbonate through the coating of red pint (Fig. 7).

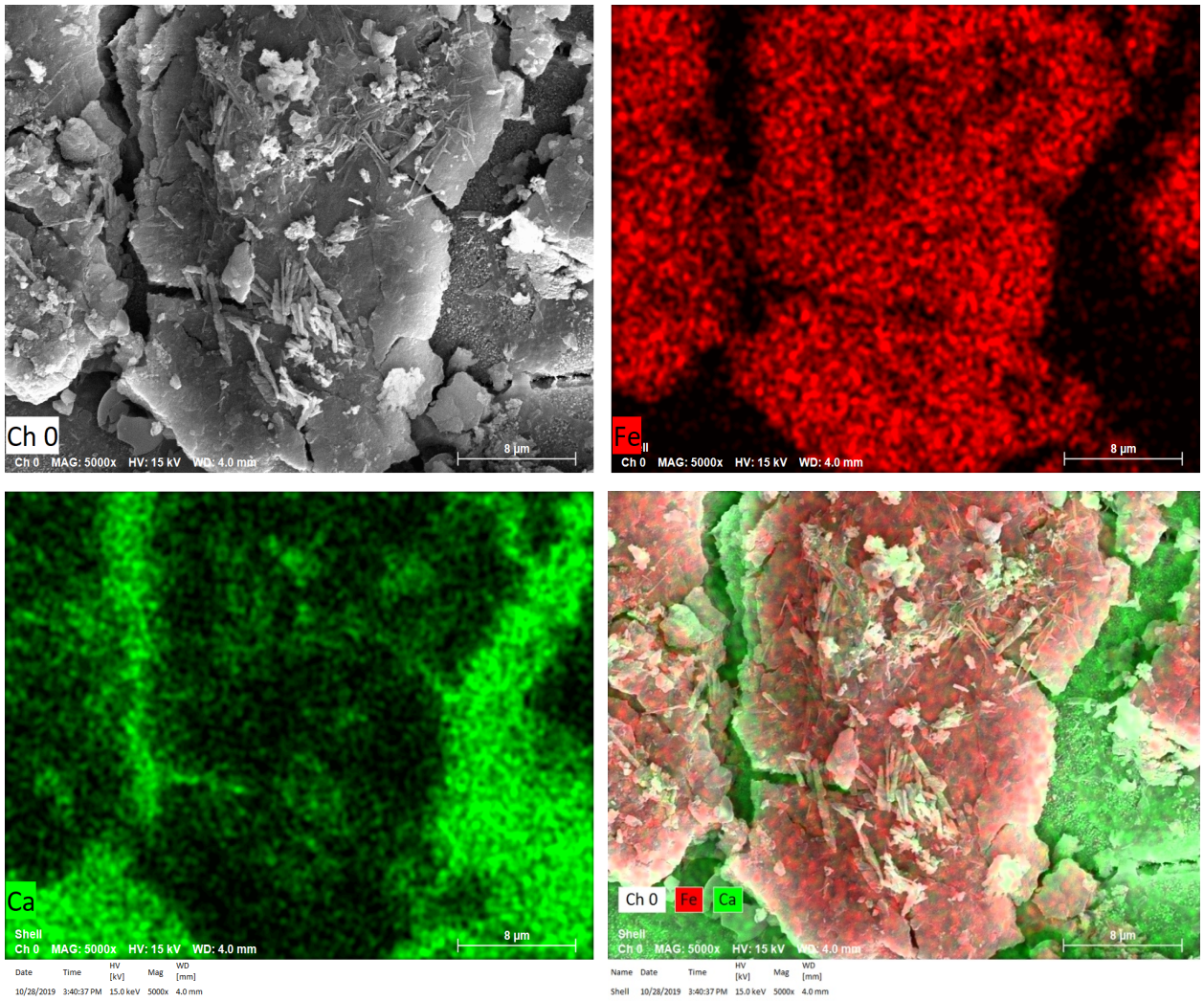

Figure 7: SEM images of red layer of shell with iron concentrated displayed in red and calcium in green

Conclusions:

Iron oxides often will change form over time or under exposure to light, especially common under the focused beam of the Raman spectrometer, making it challenging to narrow down original molecular structure. However, the dirt and shell analyzed in this study nonetheless displayed very distinct molecules. Hematite, found in the soil, is the most common and stable form of iron oxide, used at other Oneota sites for painting wall designs and objects, most often

pottery.[21] However, the goethite layer on the surface of these shells is a feasible source, especially consistent to the region surrounding Middle Grant Creek. Goethite is the main component of bog iron ore, which, as hematite, could be ground into a pigment and applied as decoration to a surface. In fact, the Kankakee region of Illinois is said to have "near extensive bog iron ore."[22] As a result, the pigmentation of these shells could likely have been locally sourced.

Intentional coloration of the shells could indicate their role within a ritualistic context or as decorative ornamentation. A study of comparably red-colored shells from the Neanderthals of Iberia utilized similar scientific analysis to identify the pigmentation as a mixture of goethite and hematite.[23] These finds were used as evidence of body ornamentation and behavioral modernity within European Neanderthal communities, generally associated primarily with concurrent cultures of Africa.[24]

Further study could compare Raman spectra of bog iron ore found near Middle Grant Creek to the results of this study as potential evidence for locally sourced pigmentation. Additionally, analysis could be carried out on other specimens of the site containing red pigmentation to determine if they also indicate goethite as the primary form of iron within paint. For example, a block of galena lead ore also excavated at the site was likely used for ritual purposes and displayed similar fragments of red paint to the shells. Finally, a study of the kinds of specimens found in the same level of the pit as the shells could look for objects with related functions. Other decorative or ritual objects could indicate a relation in use, ownership, and original context between the shells and specimens deposited alongside it.

---

[21] Berry and Chapman, "An Oneota Site in Missouri 1," 299.
[22] Bateman et al., *Historical Encyclopedia of Illinois*, 313.
[23] Zilhão et al., "Symbolic Use of Marine Shells and Mineral Pigments by Iberian Neandertals," 1025.
[24] Zilhão et al., 1027.

References:

"Applications of Scanning Electron Microscopy in Archaeology - ScienceDirect." Accessed December 14, 2019. https://www.sciencedirect.com/science/article/pii/S006525390860904X.

Bellot-Gurlet, Ludovic, Delphine Neff, Solenn Réguer, Judith Monnier, Mandana Saheb, and Philippe Dillmann. "Raman Studies of Corrosion Layers Formed on Archaeological Irons in Various Media." Journal of Nano Research, 2009. https://doi.org/10.4028/www.scientific.net/JNanoR.8.147.

Berry, Brewton, and Carl Chapman. "An Oneota Site in Missouri 1." *American Antiquity* 7, no. 3 (January 1942): 290–305. https://doi.org/10.2307/275485.

Chapman, Carl H., and Eleanor F. Chapman. *Indians and Archaeology of Missouri, Revised Edition*. University of Missouri Press, 1983.

Creagh, D. C., and D. A. Bradley. *Radiation in Art and Archeometry*. 1 edition. Amsterdam ; New York: Elsevier Science, 2000.

Frahm, Ellery. "Scanning Electron Microscopy (SEM)." In *Encyclopedia of Geoarchaeology*, edited by Allan S. Gilbert, 755–64. Dordrecht: Springer Netherlands, 2017. https://doi.org/10.1007/978-1-4020-4409-0_25.

"Hematite R070240 - RRUFF Database: Raman, X-Ray, Infrared, and Chemistry." Accessed December 14, 2019. http://rruff.info/hematite/display=raman/R070240.

Luna, Aderval S., Igor C. A. Lima, Werickson F. C. Rocha, Joyce R. Araújo, Alexei Kuznetsov, Erlon H. Martins Ferreira, Ricard Boqué, and Joan Ferré. "Classification of Soil Samples Based on Raman Spectroscopy and X-Ray Fluorescence Spectrometry Combined with

Chemometric Methods and Variable Selection." *Analytical Methods* 6, no. 22 (October 23, 2014): 8930–39. https://doi.org/10.1039/C4AY01967A.

Marucci, G., A. Beeby, A. W. Parker, and C. E. Nicholson. "Raman Spectroscopic Library of Medieval Pigments Collected with Five Different Wavelengths for Investigation of Illuminated Manuscripts." *Analytical Methods* 10, no. 10 (2018): 1219–36. https://doi.org/10.1039/C8AY00016F.

McLeester, Madeleine, Mark R. Schurr, Katherine M. Sterner, and Robert E. Ahlrichs. "Protohistoric Marine Shell Working: New Evidence from Northern Illinois." *American Antiquity* 84, no. 3 (July 2019): 549–58. https://doi.org/10.1017/aaq.2019.44.

Pauketat, Timothy. *The Oxford Handbook of North American Archaeology*. Oxford University Press, 2015.

Rzepa, Grzegorz, Tomasz Bajda, Adam Gaweł, Klaudia Debiec, and Lukasz Drewniak. "Mineral Transformations and Textural Evolution during Roasting of Bog Iron Ores." *Journal of Thermal Analysis and Calorimetry* 123, no. 1 (January 1, 2016): 615–30. https://doi.org/10.1007/s10973-015-4925-1.

Shackley, M. Steven, ed. *X-Ray Fluorescence Spectrometry (XRF) in Geoarchaeology*. New York: Springer-Verlag, 2011. https://doi.org/10.1007/978-1-4419-6886-9.

Theler, James L., and Robert F. Boszhardt. *Twelve Millennia: Archaeology of the Upper Mississippi River Valley*. University of Iowa Press, 2005.

Townsend, Richard F. *Hero, Hawk, and Open Hand: American Indian Art of the Ancient Midwest and South*. Yale University Press, 2004.

Zilhão, João, Diego E. Angelucci, Ernestina Badal-García, Francesco d'Errico, Floréal Daniel, Laure Dayet, Katerina Douka, et al. "Symbolic Use of Marine Shells and Mineral Pigments

by Iberian Neandertals." *Proceedings of the National Academy of Sciences* 107, no. 3 (January 19, 2010): 1023–28. https://doi.org/10.1073/pnas.0914088107.

Appendices:

Appendix A: X-ray Fluorescence (XRF) Data

Shell A: Exterior

Element	Wt%	At%
AlK	0.70	1.04
SiK	3.57	5.10
K K	0.02	0.02
CaK	88.37	88.55
TiK	0.09	0.08
MnK	0.06	0.05
FeK	7.19	5.17

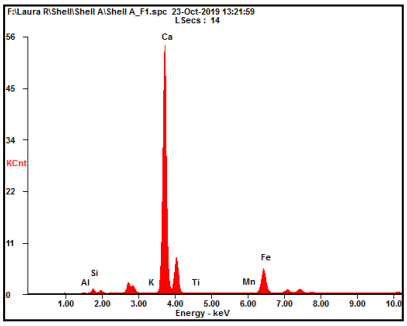

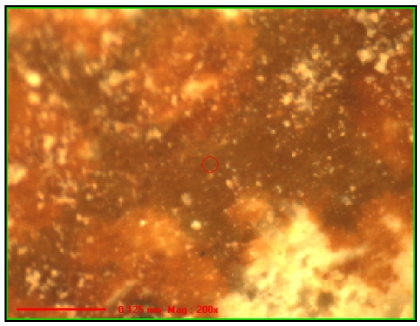

Element	Wt%	At%
AlK	0.40	0.60
SiK	0.48	0.68
K K	0.02	0.02
CaK	98.49	98.26
TiK	0.06	0.05
MnK	0.11	0.08
FeK	0.43	0.31

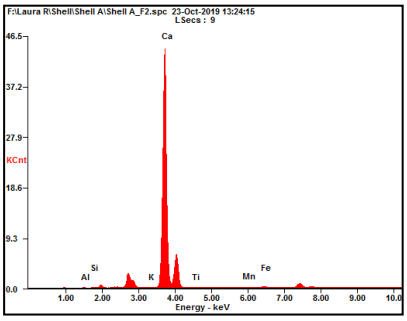

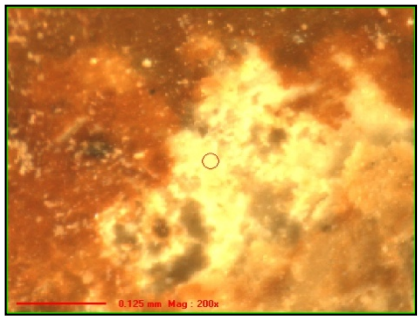

Element	Wt%	At%
AlK	11.70	13.59
SiK	58.85	65.66
K K	5.49	4.40
CaK	12.65	9.89
TiK	1.12	0.74
MnK	0.41	0.24
FeK	9.77	5.48

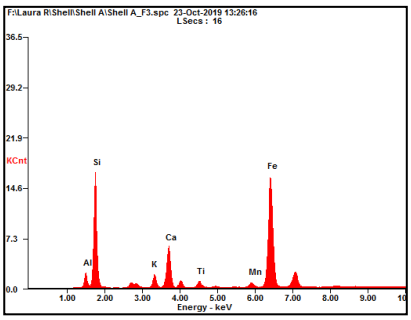

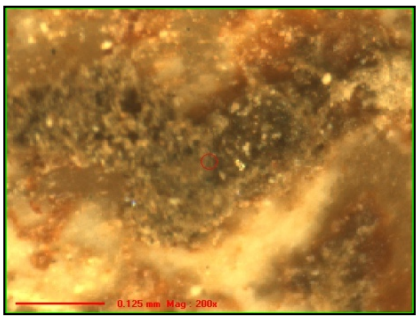

Element	Wt%	At%
AlK	0.25	0.37
SiK	0.08	0.12
K K	0.02	0.02
CaK	98.68	98.78
TiK	0.07	0.06
MnK	0.47	0.34
FeK	0.43	0.31

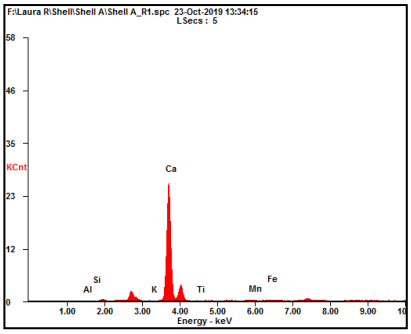

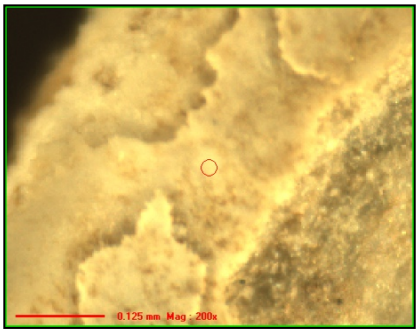

Element	Wt%	At%
AlK	0.24	0.36
SiK	0.30	0.42
K K	0.02	0.02
CaK	98.51	98.51
TiK	0.08	0.06
MnK	0.60	0.44
FeK	0.25	0.18

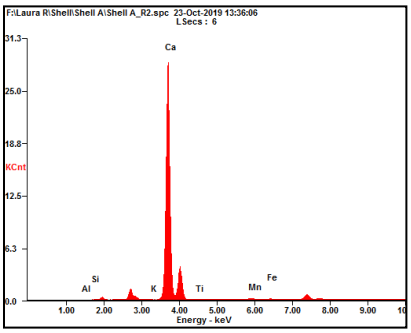

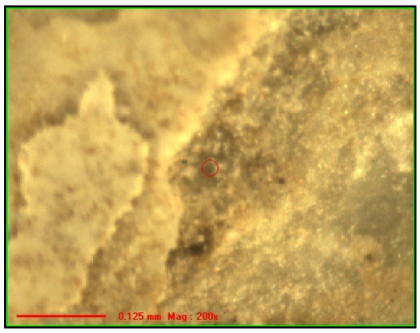

Element	Wt%	At%
AlK	4.64	6.46
SiK	11.51	15.39
K K	0.59	0.57
CaK	81.49	76.37
TiK	0.16	0.12
MnK	0.24	0.16
FeK	1.38	0.93

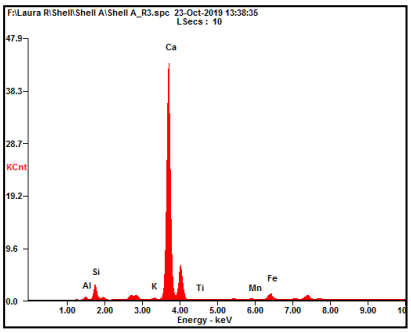

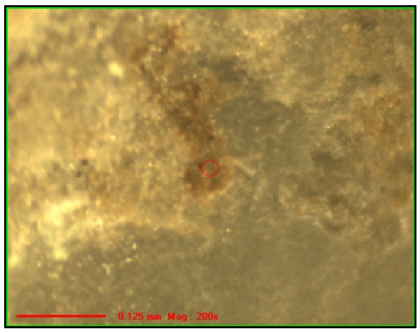

Shell B: Exterior

Element	Wt%	At%
AlK	2.75	3.94
SiK	6.72	9.26
K K	0.19	0.19
CaK	87.93	84.92
TiK	0.15	0.12
MnK	0.24	0.17
FeK	2.04	1.41

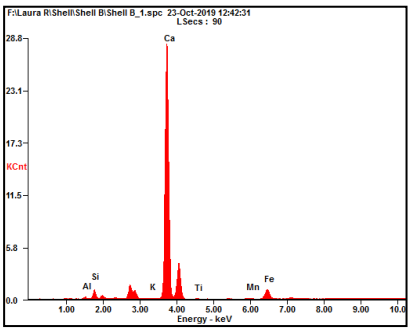

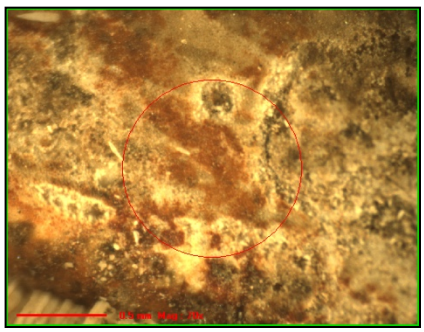

Element	Wt%	At%
AlK	2.48	3.59
SiK	6.45	8.97
K K	0.16	0.16
CaK	86.02	83.84
TiK	0.18	0.15
MnK	0.13	0.09
FeK	4.58	3.20

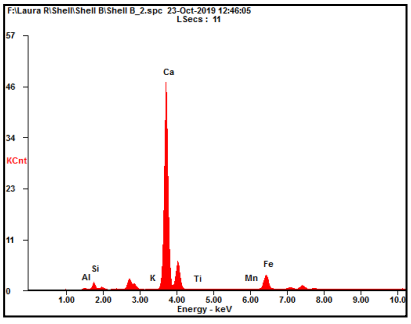

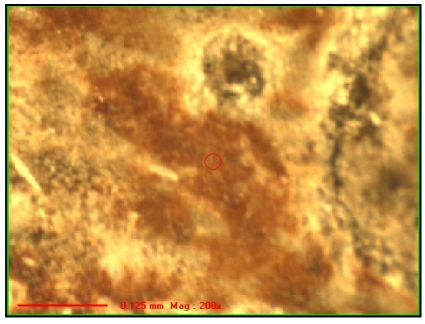

Shell B: Interior

Element	Wt%	At%
AlK	0.56	0.83
SiK	0.81	1.15
K K	0.06	0.06
CaK	98.24	97.72
TiK	0.02	0.02
MnK	0.21	0.16
FeK	0.09	0.06

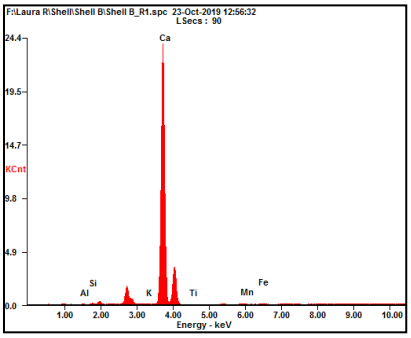

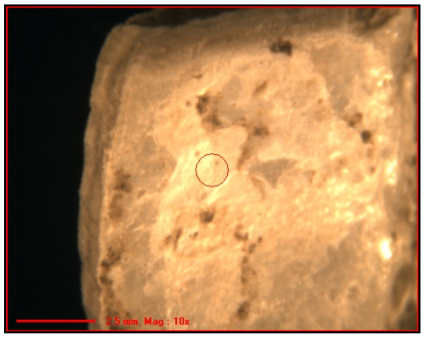

Element	Wt%	At%
AlK	1.07	1.57
SiK	1.90	2.68
K K	0.10	0.10
CaK	96.49	95.33
TiK	0.04	0.04
MnK	0.23	0.16
FeK	0.18	0.13

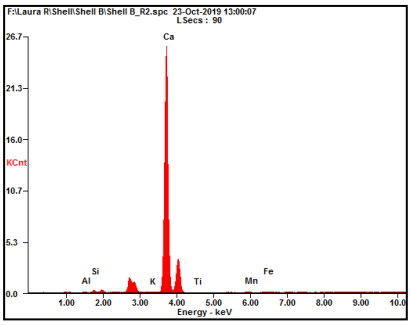

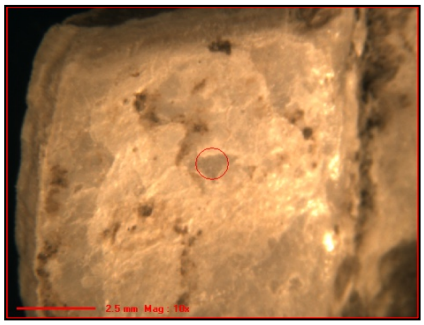

Soil Sample: Level 13

Element	Wt%	At%
AlK	10.35	11.85
SiK	64.31	70.74
K K	5.03	3.97
CaK	9.65	7.44
TiK	1.14	0.73
MnK	0.32	0.18
FeK	9.14	5.06
ZnK	0.06	0.03

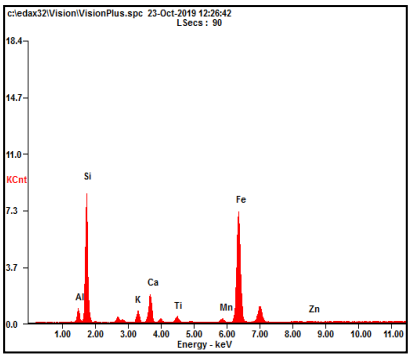

Element	Wt%	At%
AlK	11.78	13.28
SiK	66.88	72.43
K K	5.30	4.13
CaK	6.19	4.70
TiK	1.07	0.68
MnK	0.38	0.21
FeK	8.40	4.58

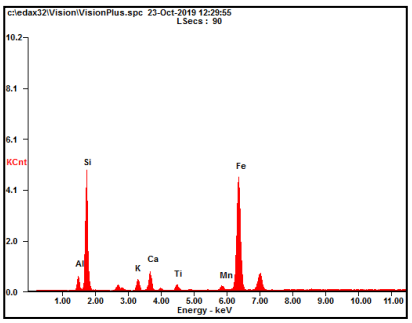

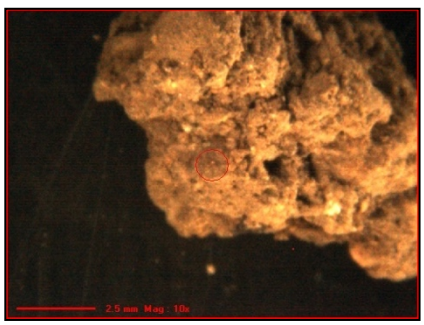

Soil Sample: Level 8

Element	Wt%	At%
AlK	3.97	5.38
SiK	19.35	25.19
P K	3.18	3.76
K K	2.21	2.06
CaK	65.37	59.65
TiK	0.63	0.48
MnK	0.58	0.39
FeK	4.63	3.03
ZnK	0.08	0.04

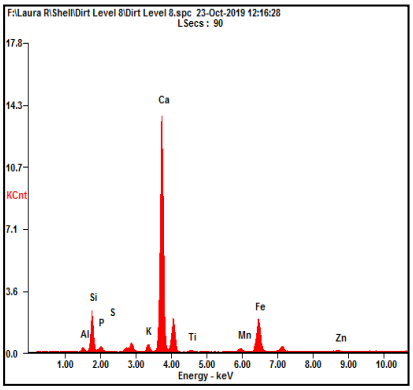

Soil Sample: Level 9

Element	Wt%	At%
AlK	10.78	12.06
SiK	70.55	75.83
K K	5.27	4.07
CaK	3.25	2.45
TiK	1.20	0.76
MnK	0.29	0.16
FeK	8.60	4.65
ZnK	0.05	0.02

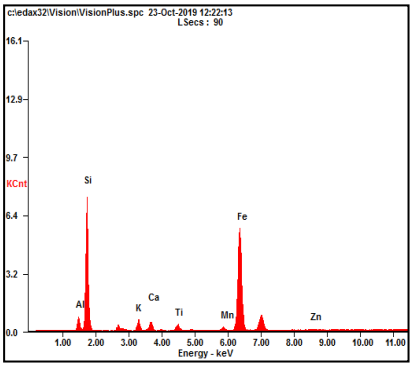

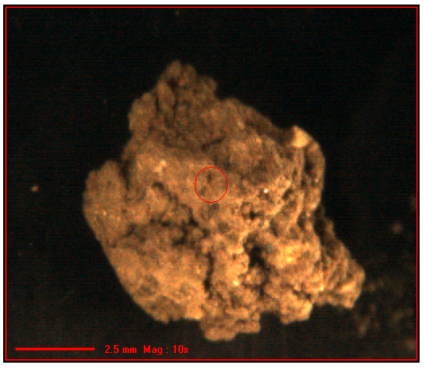

Appendix B: Raman Data

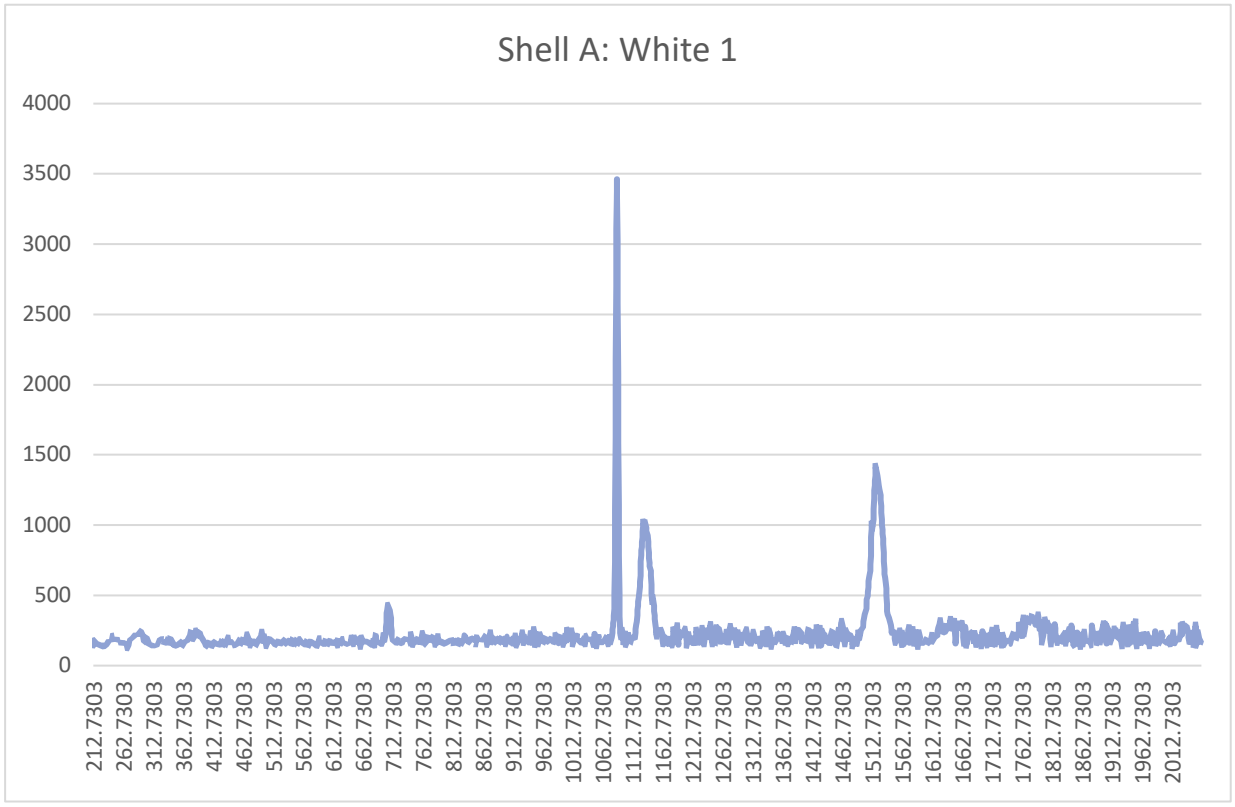

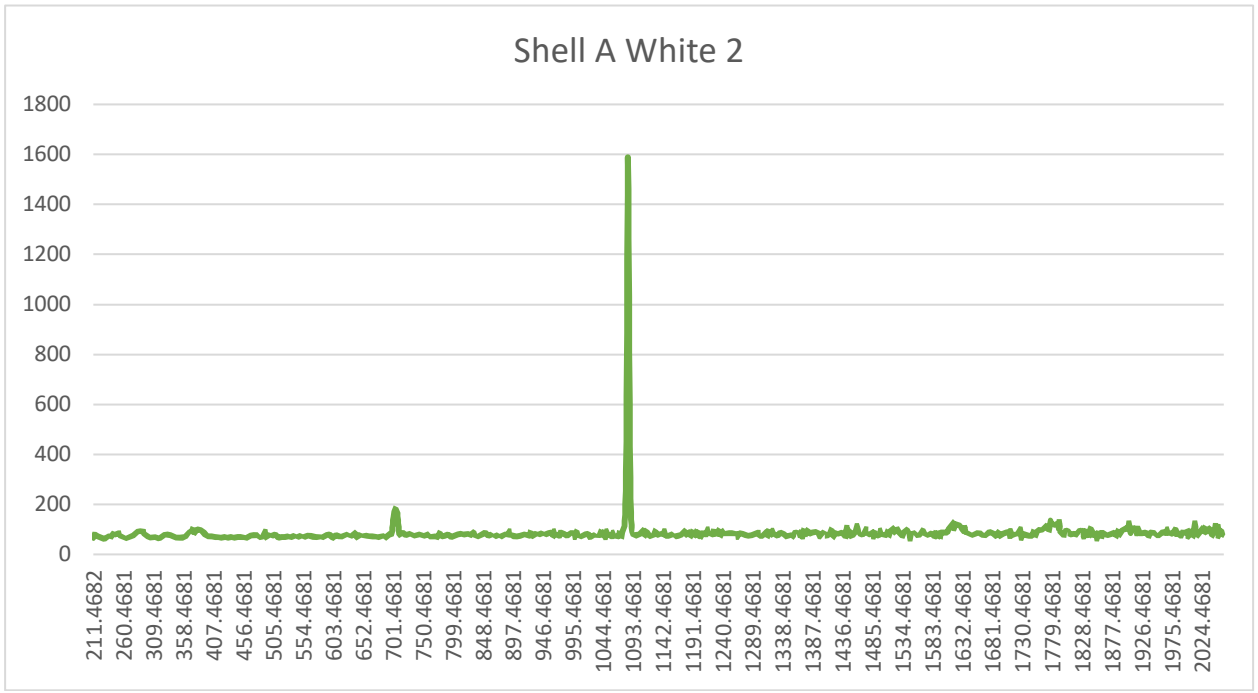

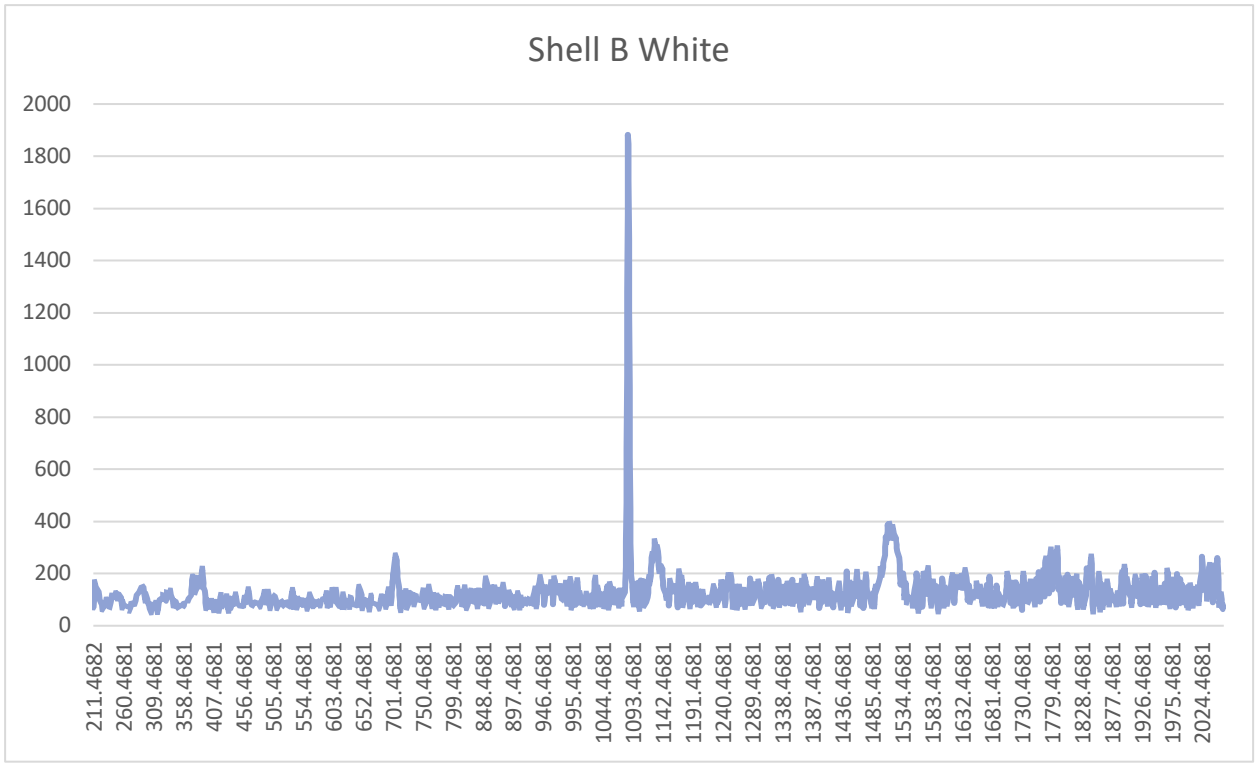
Shell B White
2000
1800
1600
1400
1200
1000
800
600
400
200
0
211.4682
260.4681
309.4681
358.4681
407.4681
456.4681
505.4681
554.4681
603.4681
652.4681
701.4681
750.4681
799.4681
848.4681
897.4681
946.4681
995.4681
1044.4681
1093.4681
1142.4681
1191.4681
1240.4681
1289.4681
1338.4681
1387.4681
1436.4681
1485.4681
1534.4681
1583.4681
1632.4681
1681.4681
1730.4681
1779.4681
1828.4681
1877.4681
1926.4681
1975.4681
2024.4681

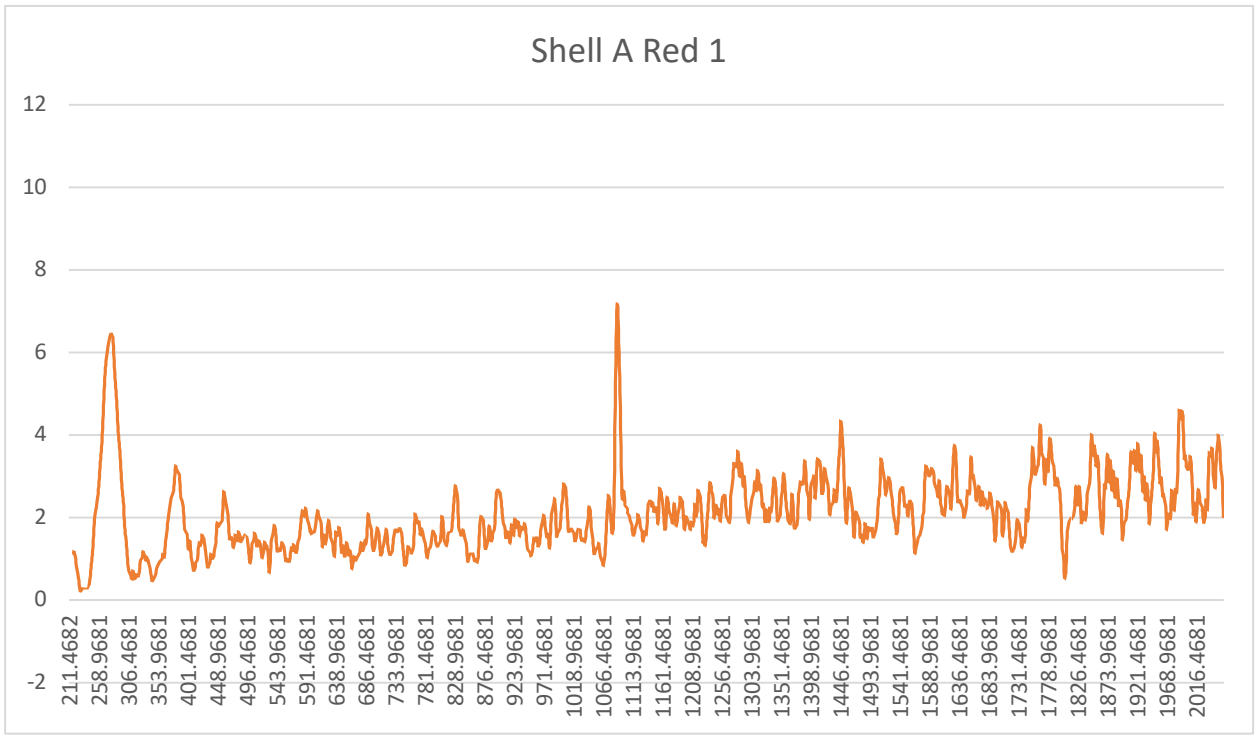
Shell A Red 1
12
10
8
6
4
2
0
-2
211.4682
258.9681
306.4681
353.9681
401.4681
448.9681
496.4681
543.9681
591.4681
638.9681
686.4681
733.9681
781.4681
828.9681
876.4681
923.9681
971.4681
1018.9681
1066.4681
1113.9681
1161.4681
1208.9681
1256.4681
1303.9681
1351.4681
1398.9681
1446.4681
1493.9681
1541.4681
1588.9681
1636.4681
1683.9681
1731.4681
1778.9681
1826.4681
1873.9681
1921.4681
1968.9681
2016.4681

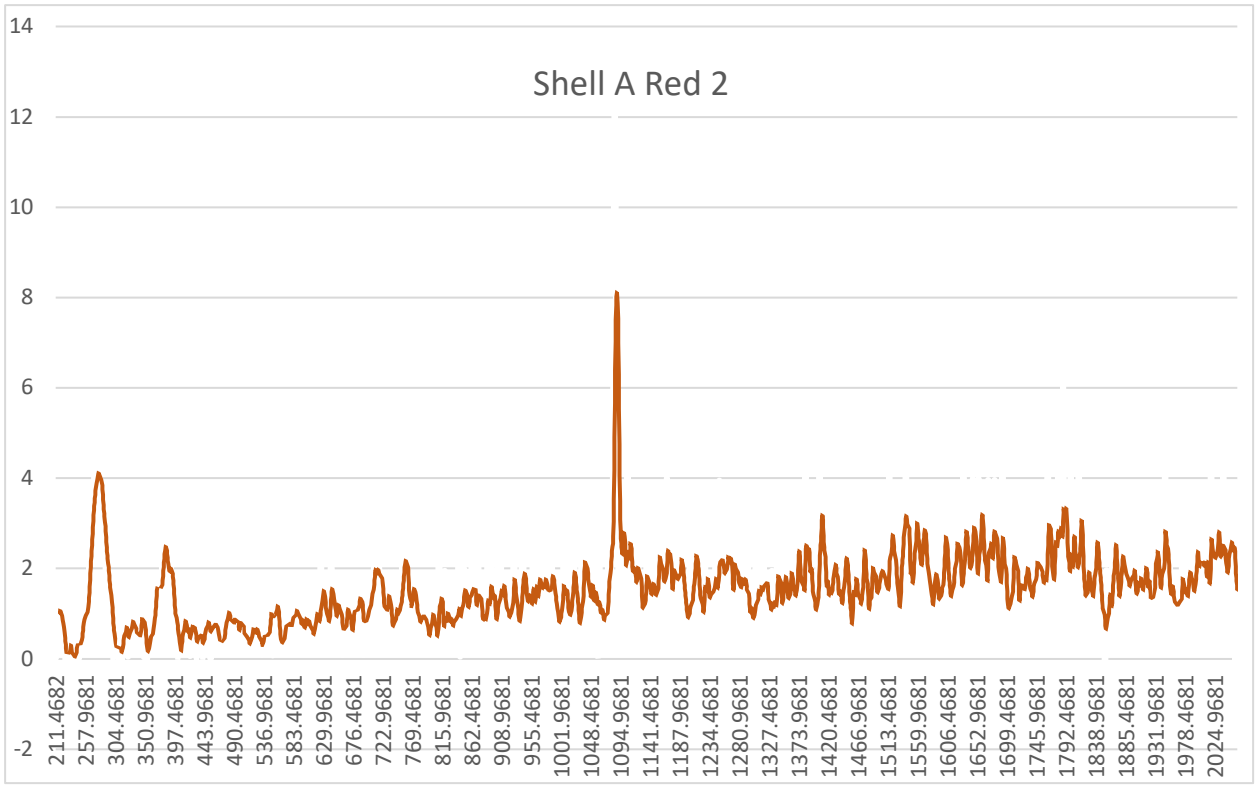
Shell A Red 2
14
12
10
8
6
4
2
0
-2
211.4682
257.9681
304.4681
350.9681
397.4681
443.9681
490.4681
536.9681
583.4681
629.9681
676.4681
722.9681
769.4681
815.9681
862.4681
908.9681
955.4681
1001.9681
1048.4681
1094.9681
1141.4681
1187.9681
1234.4681
1280.9681
1327.4681
1373.9681
1420.4681
1466.9681
1513.4681
1559.9681
1606.4681
1652.9681
1699.4681
1745.9681
1792.4681
1838.9681
1885.4681
1931.9681
1978.4681
2024.9681

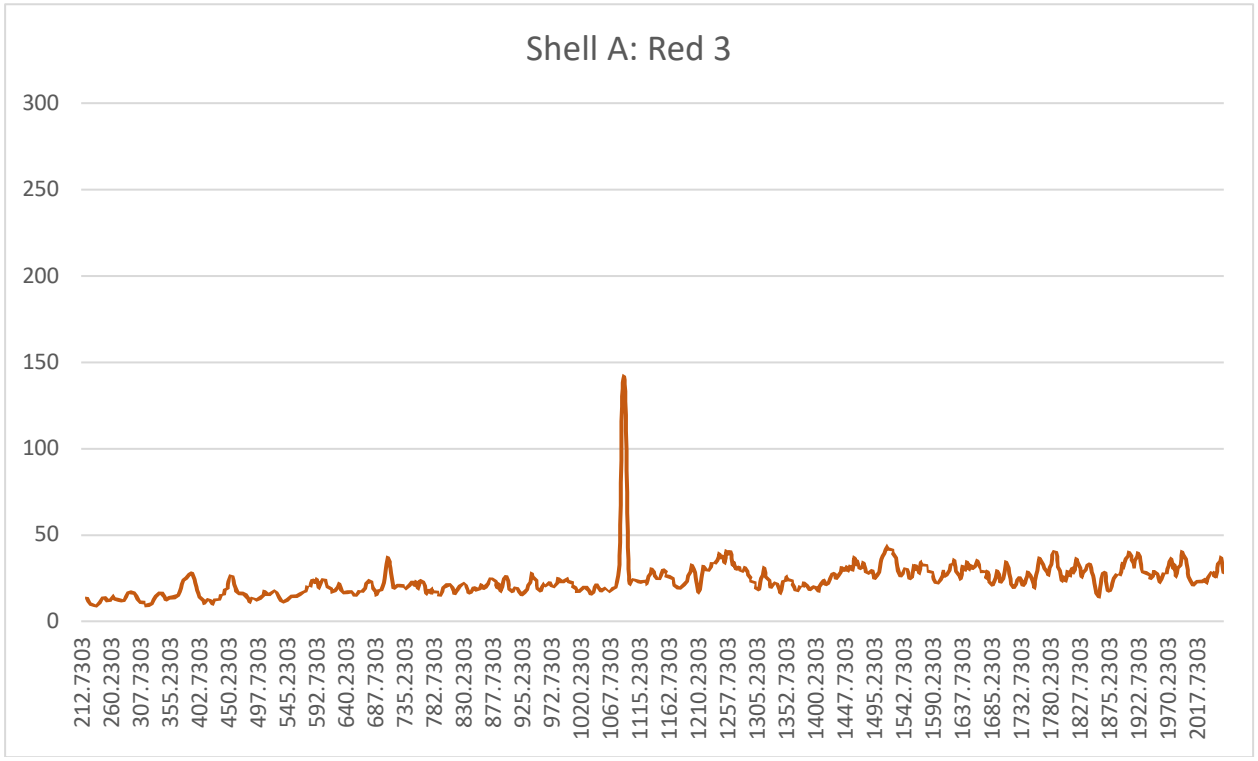
Shell A: Red 3
300
250
200
150
100
50
0
212.7303
260.2303
307.7303
355.2303
402.7303
450.2303
497.7303
545.2303
592.7303
640.2303
687.7303
735.2303
782.7303
830.2303
877.7303
925.2303
972.7303
1020.2303
1067.7303
1115.2303
1162.7303
1210.2303
1257.7303
1305.2303
1352.7303
1400.2303
1447.7303
1495.2303
1542.7303
1590.2303
1637.7303
1685.2303
1732.7303
1780.2303
1827.7303
1875.2303
1922.7303
1970.2303
2017.7303

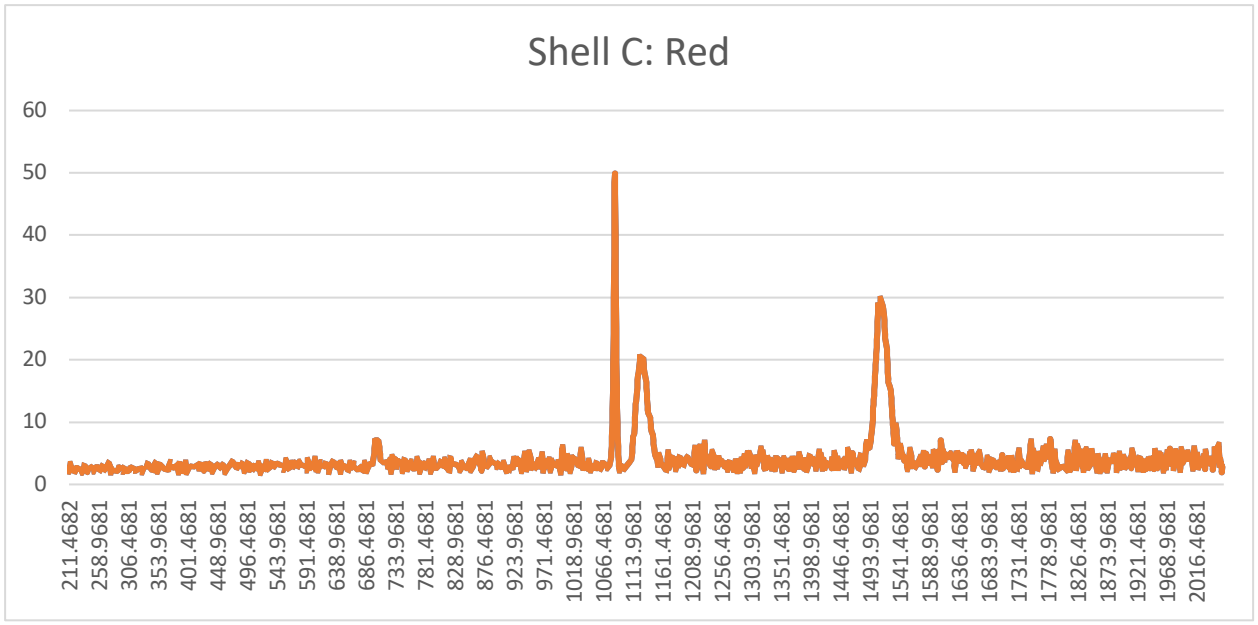
Shell C: Red
60
50
40
30
20
10
0
211.4682
258.9681
306.4681
353.9681
401.4681
448.9681
496.4681
543.9681
591.4681
638.9681
686.4681
733.9681
781.4681
828.9681
876.4681
923.9681
971.4681
1018.9681
1066.4681
1113.9681
1161.4681
1208.9681
1256.4681
1303.9681
1351.4681
1398.9681
1446.4681
1493.9681
1541.4681
1588.9681
1636.4681
1683.9681
1731.4681
1778.9681
1826.4681
1873.9681
1921.4681
1968.9681
2016.4681

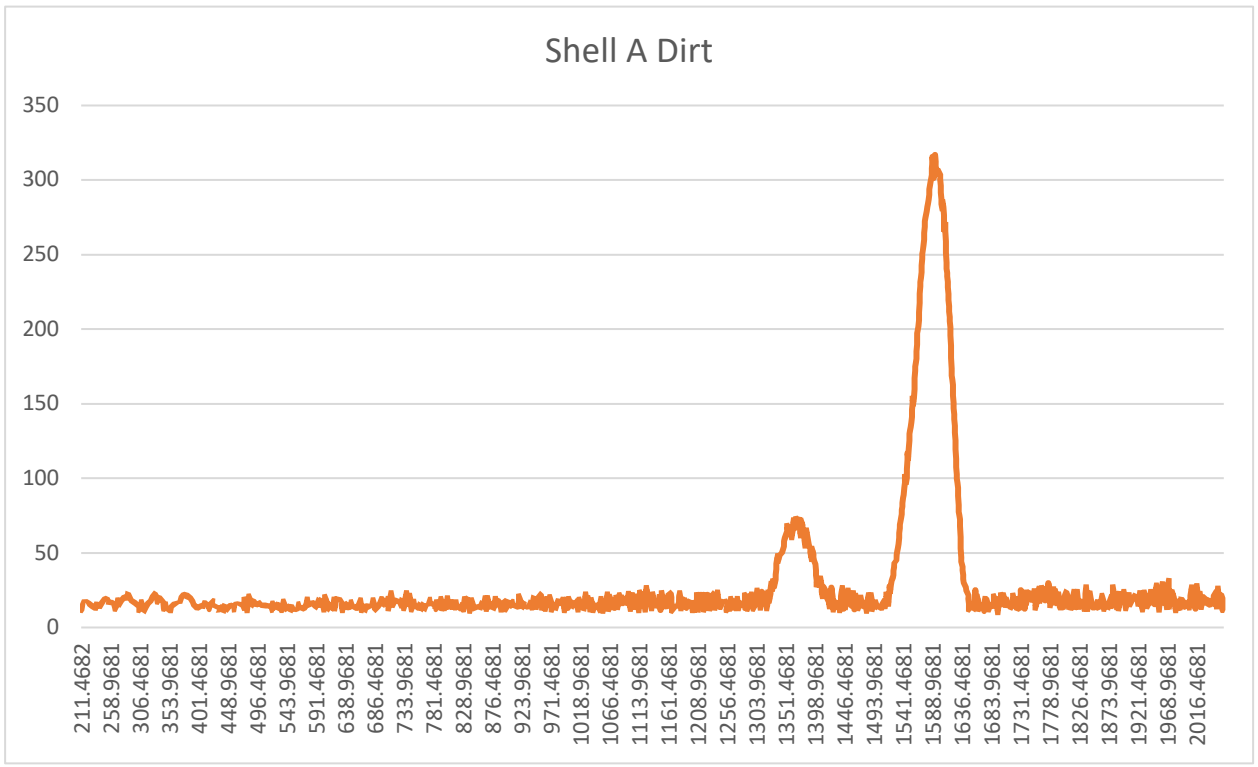
Shell A Dirt
350
300
250
200
150
100
50
0
211.4682
258.9681
306.4681
353.9681
401.4681
448.9681
496.4681
543.9681
591.4681
638.9681
686.4681
733.9681
781.4681
828.9681
876.4681
923.9681
971.4681
1018.9681
1066.4681
1113.9681
1161.4681
1208.9681
1256.4681
1303.9681
1351.4681
1398.9681
1446.4681
1493.9681
1541.4681
1588.9681
1636.4681
1683.9681
1731.4681
1778.9681
1826.4681
1873.9681
1921.4681
1968.9681
2016.4681

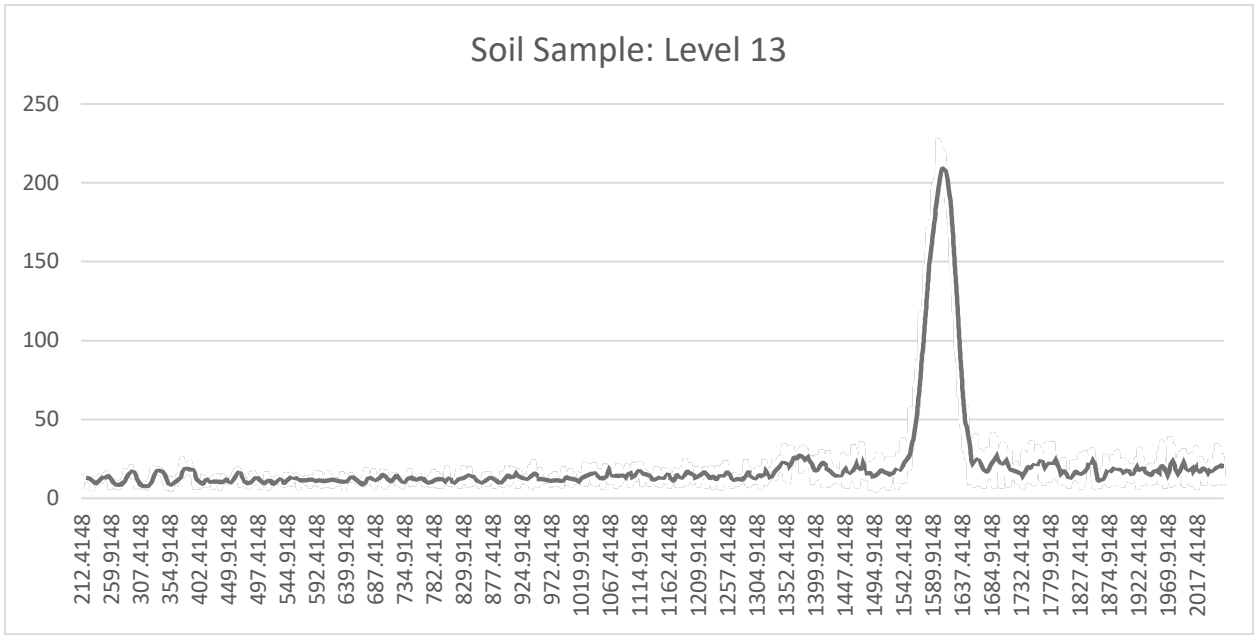
Soil Sample: Level 13
250
200
150
100
50
0
212.4148
259.9148
307.4148
354.9148
402.4148
449.9148
497.4148
544.9148
592.4148
639.9148
687.4148
734.9148
782.4148
829.9148
877.4148
924.9148
972.4148
1019.9148
1067.4148
1114.9148
1162.4148
1209.9148
1257.4148
1304.9148
1352.4148
1399.9148
1447.4148
1494.9148
1542.4148
1589.9148
1637.4148
1684.9148
1732.4148
1779.9148
1827.4148
1874.9148
1922.4148
1969.9148
2017.4148

Appendix 3: SEM Data

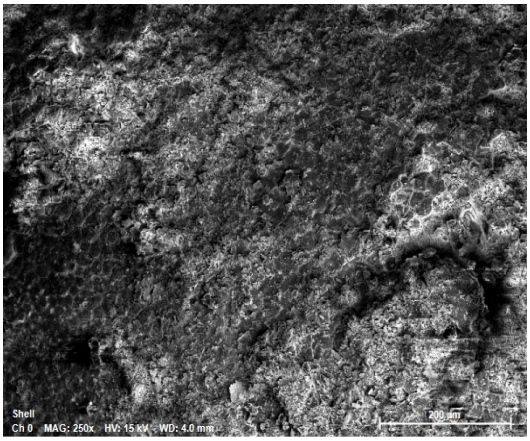

Name	Date	Time	HV [kV]	Mag	WD [mm]
Ch 0	10/28/2019	2:06:36 PM	15.0 keV	250x	4.0 mm

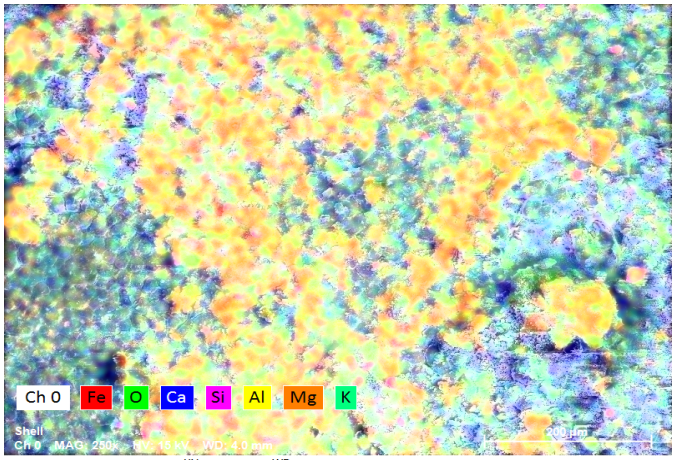

Name	Date	Time	HV [kV]	Mag	WD [mm]
Shell	10/28/2019	2:06:37 PM	15.0 keV	250x	4.0 mm

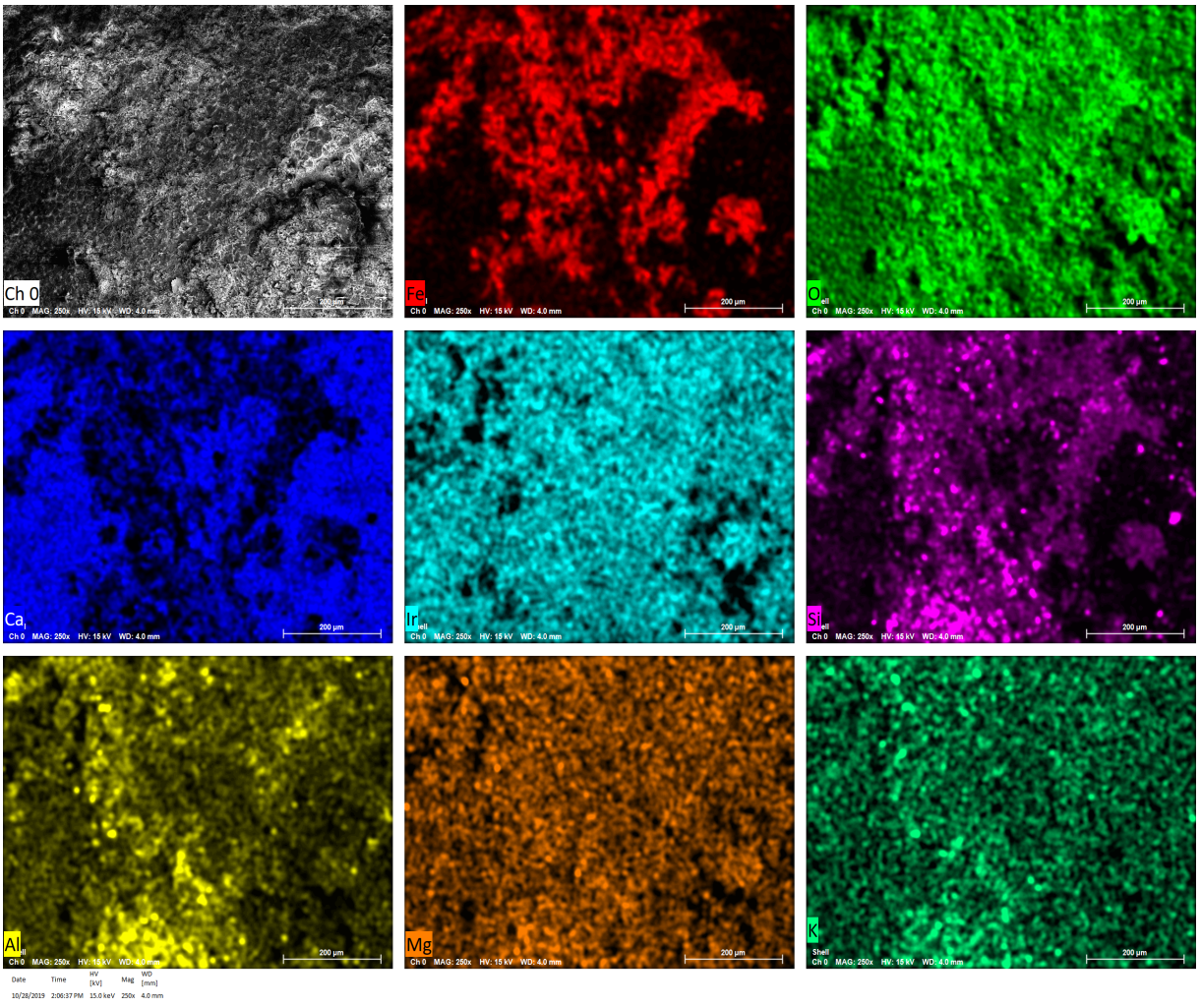

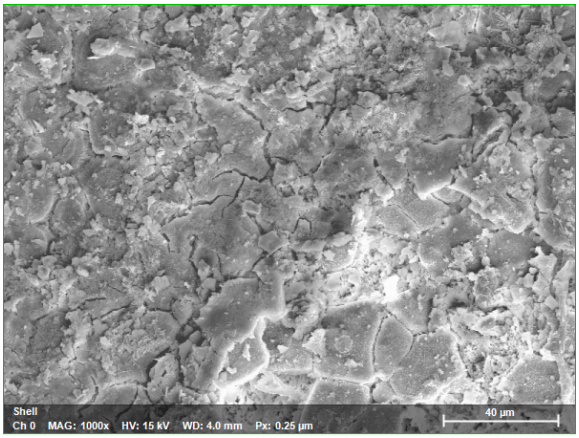

Name	Date	Time	HV [kV]	Mag	WD [mm]
Shell	10/28/2019	2:15:09 PM	15.0 keV	1000x	4.0 mm

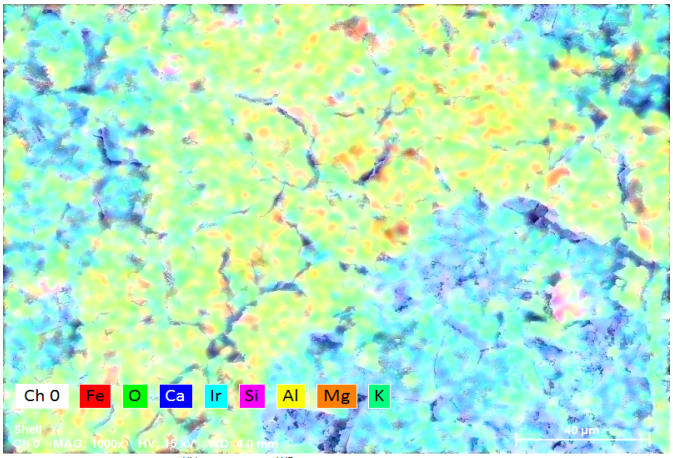

Name	Date	Time	HV [kV]	Mag	WD [mm]
Shell	10/28/2019	2:15:22 PM	15.0 keV	1000x	4.0 mm

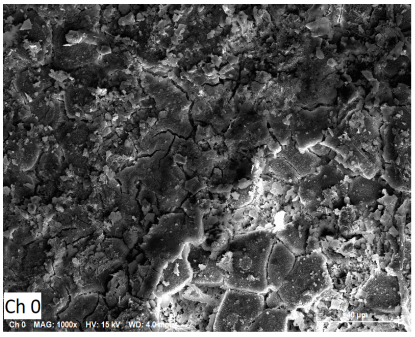

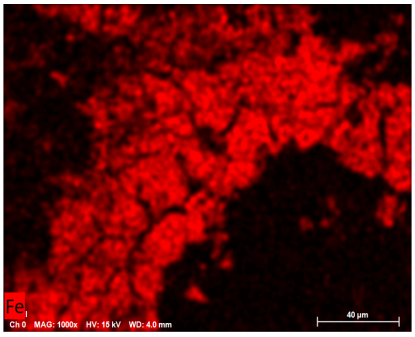

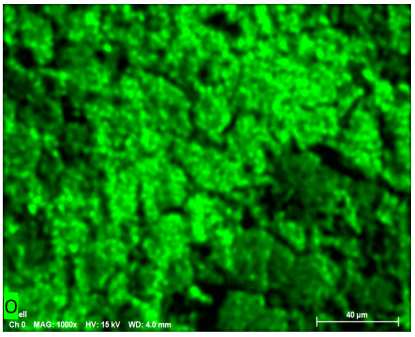

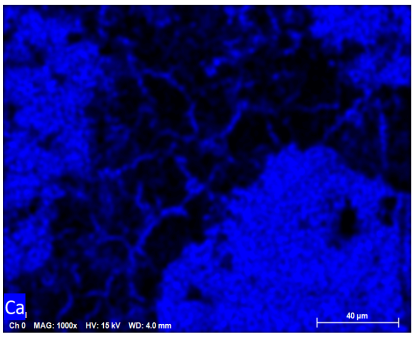

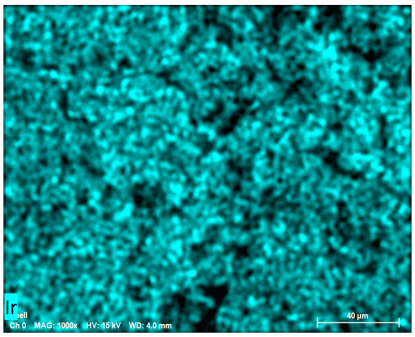

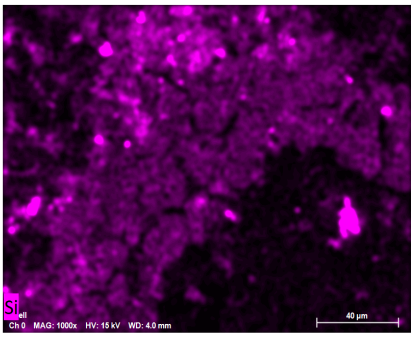

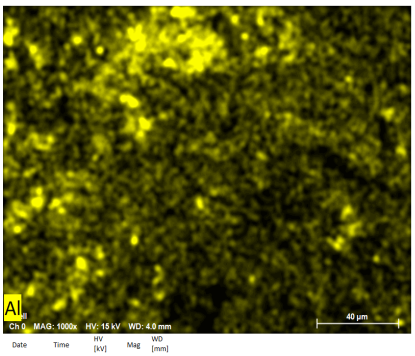

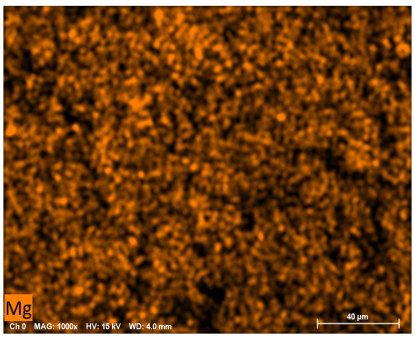

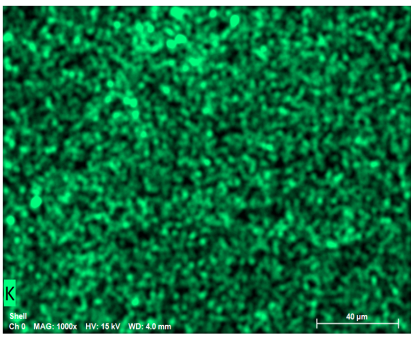

Date	Time	HV [kV]	Mag	WD [mm]
10/28/2019	2:15:22 PM	15.0 keV	1000x	4.0 mm

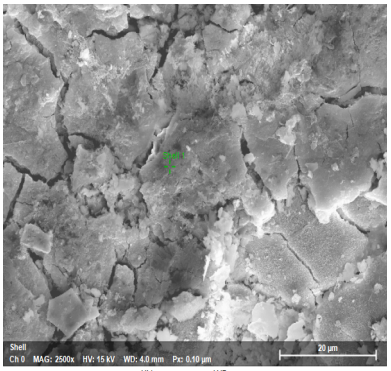

Name	Date	Time	HV [kV]	Mag	WD [mm]
Shell	10/28/2019	2:18:36 PM	15.0 keV	2500x	4.0 mm

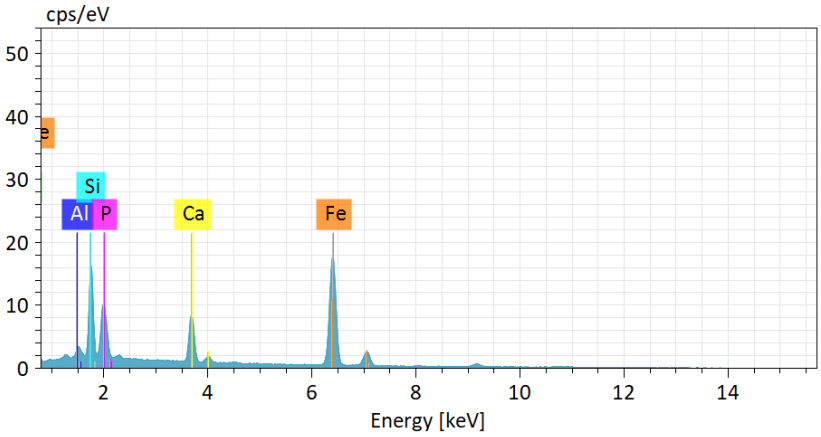

Shell 1

Element	At. No.	Netto	Mass [%]	Mass Norm. [%]	Atom [%]	abs. error [%] (1 sigma)	rel. error [%] (1 sigma)
Oxygen	8	85397	21.57	31.07	49.81	2.48	11.48
Iron	26	84475	36.46	52.52	24.12	1.10	3.01
Carbon	6	9643	6.36	9.16	19.55	0.92	14.47
Silicon	14	40501	4.86	7.00	6.39	0.23	4.72
Titanium	22	768	0.17	0.24	0.13	0.03	19.78
		Sum	**69.43**	**100.00**	**100.00**		

Name	Date	Time	HV [kV]	Mag	WD [mm]
Shell	10/28/2019	3:18:39 PM	15.0 keV	8000x	4.0 mm

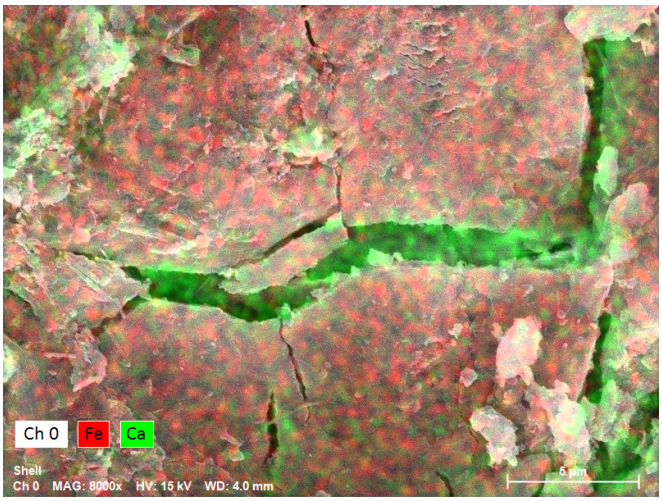

Name	Date	Time	HV [kV]	Mag	WD [mm]
Shell	10/28/2019	3:19:11 PM	15.0 keV	8000x	4.0 mm

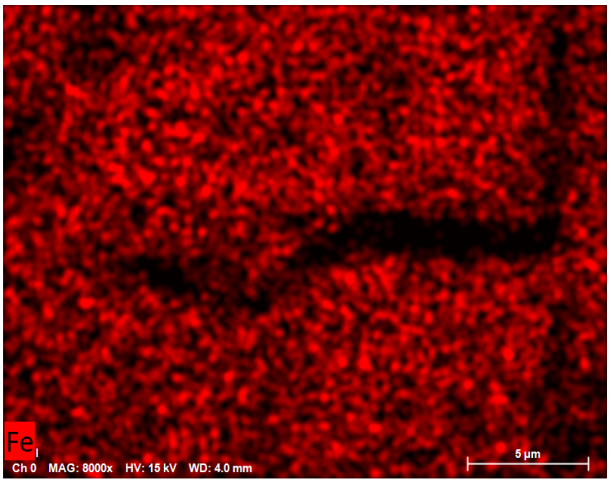

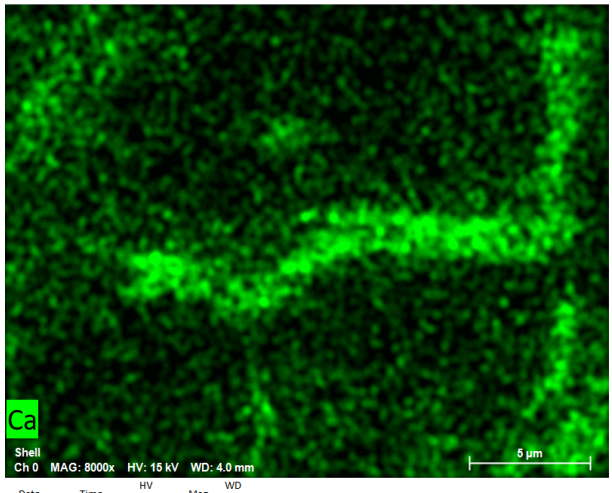

Date	Time	HV [kV]	Mag	WD [mm]
10/28/2019	3:19:11 PM	15.0 keV	8000x	4.0 mm

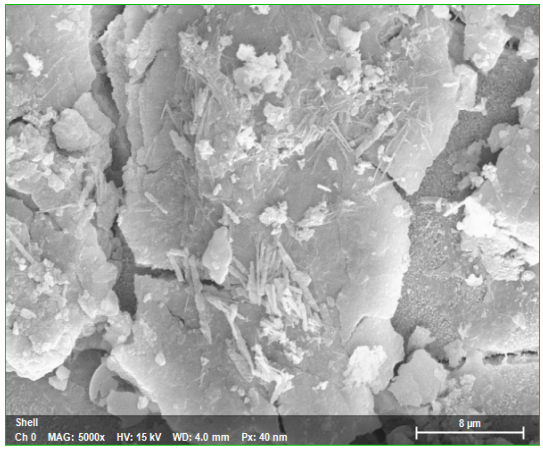

Name	Date	Time	HV [kV]	Mag	WD [mm]
Shell	10/28/2019	3:40:19 PM	15.0 keV	5000x	4.0 mm

Name	Date	Time	HV [kV]	Mag	WD [mm]
Shell	10/28/2019	3:40:37 PM	15.0 keV	5000x	4.0 mm

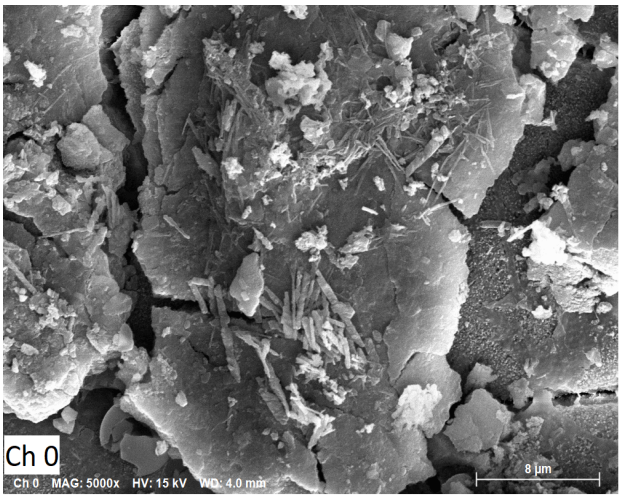

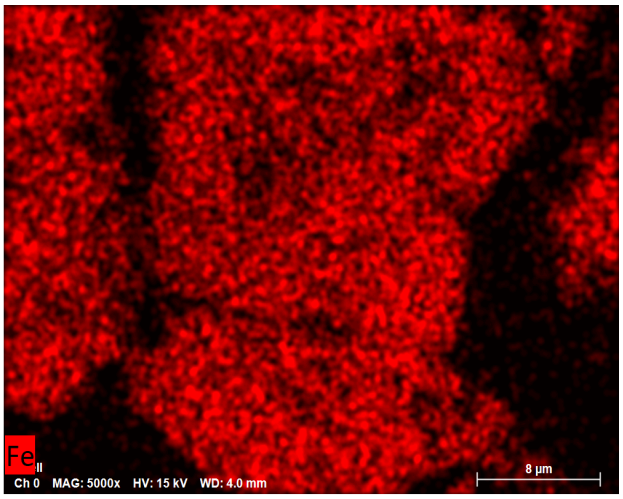

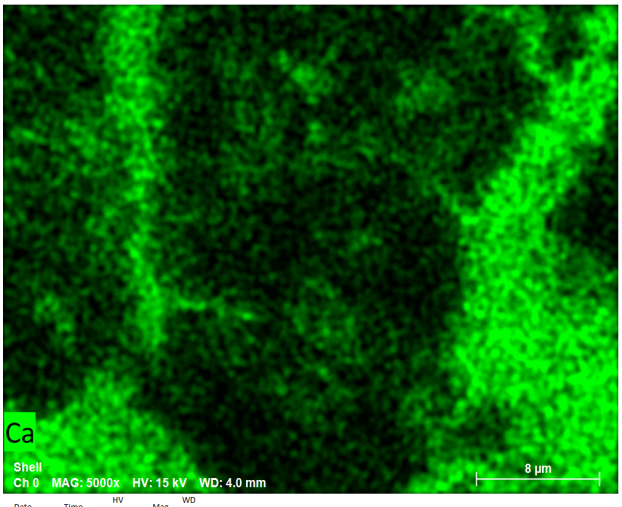

Date	Time	HV [kV]	Mag	WD [mm]
10/28/2019	3:40:37 PM	15.0 keV	5000x	4.0 mm

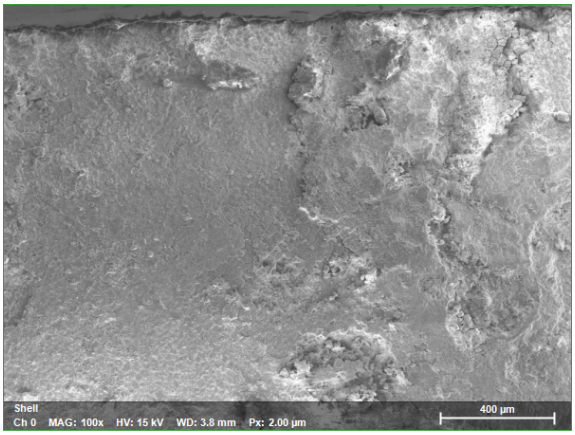

Name	Date	Time	HV [kV]	Mag	WD [mm]
Shell	10/28/2019	3:51:23 PM	15.0 keV	100x	3.8 mm

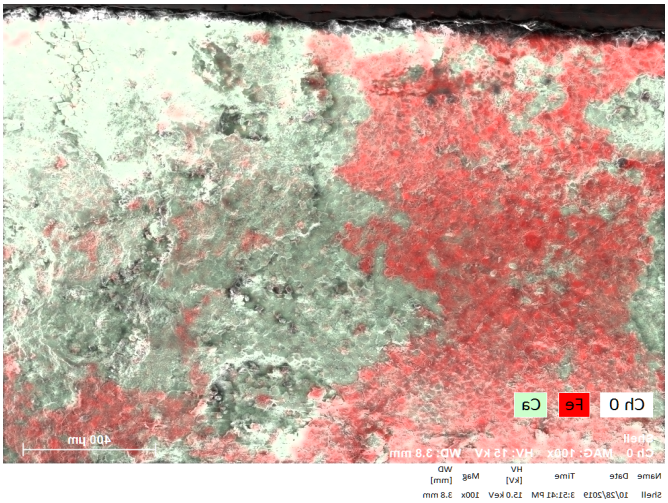

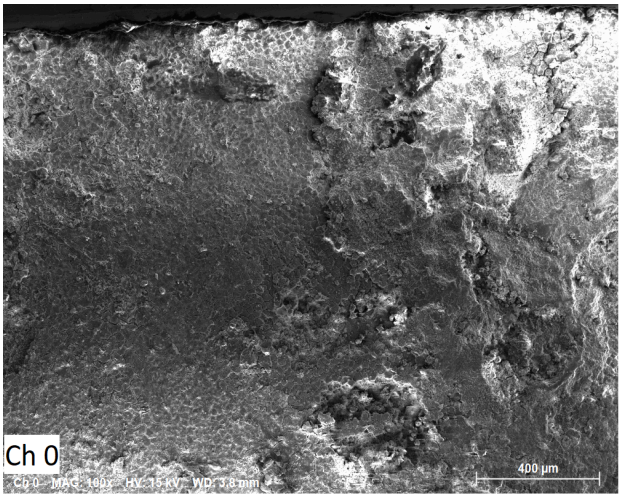

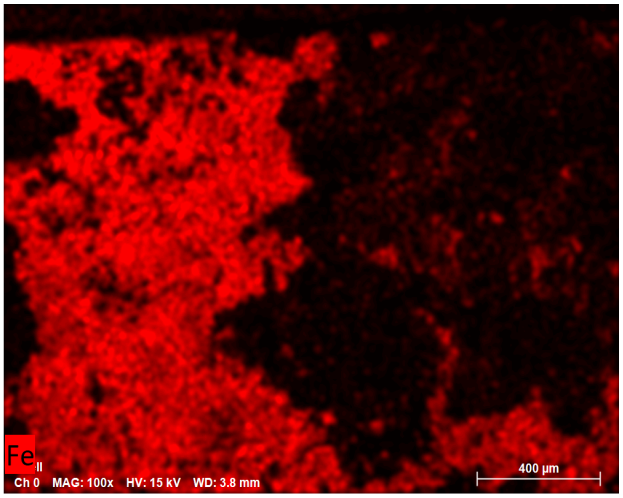

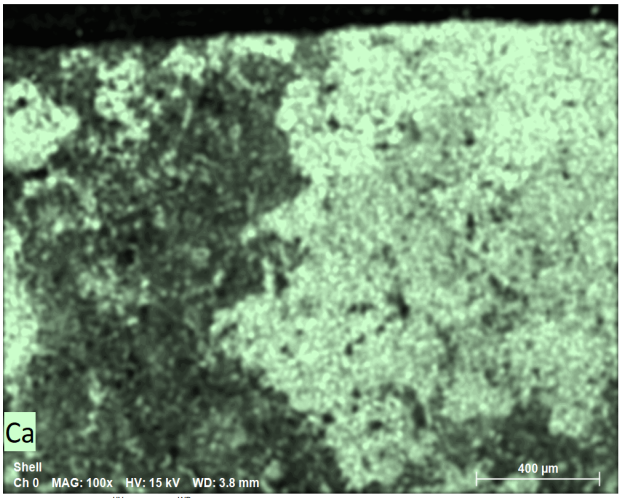

Date	Time	HV [kV]	Mag	WD [mm]
10/28/2019	3:51:41 PM	15.0 keV	100x	3.8 mm

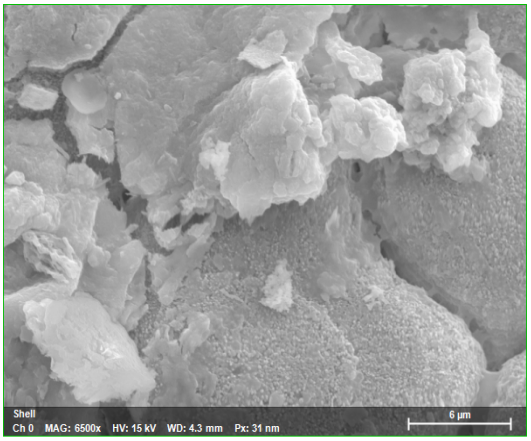

Name	Date	Time	HV [kV]	Mag	WD [mm]
Shell	10/28/2019	4:00:44 PM	15.0 keV	6500x	4.3 mm

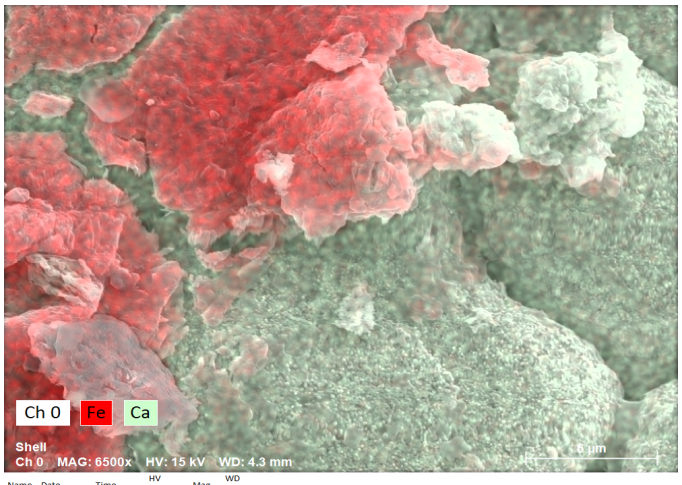

Name	Date	Time	HV [kV]	Mag	WD [mm]
Shell	10/28/2019	4:01:03 PM	15.0 keV	6500x	4.3 mm

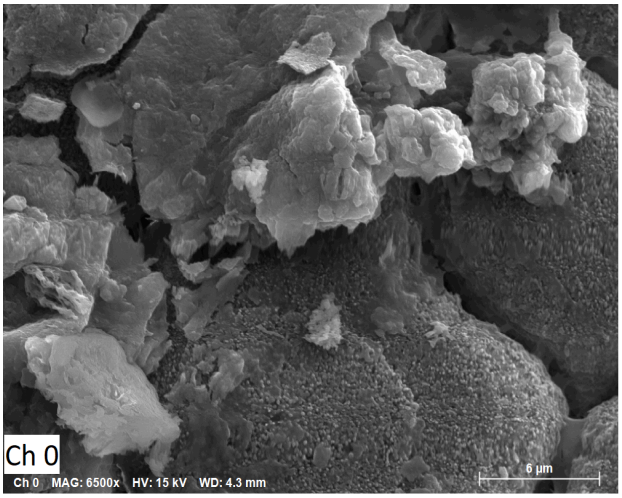

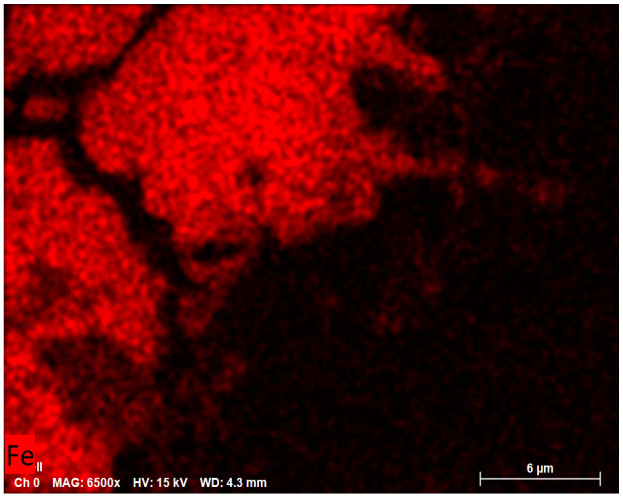

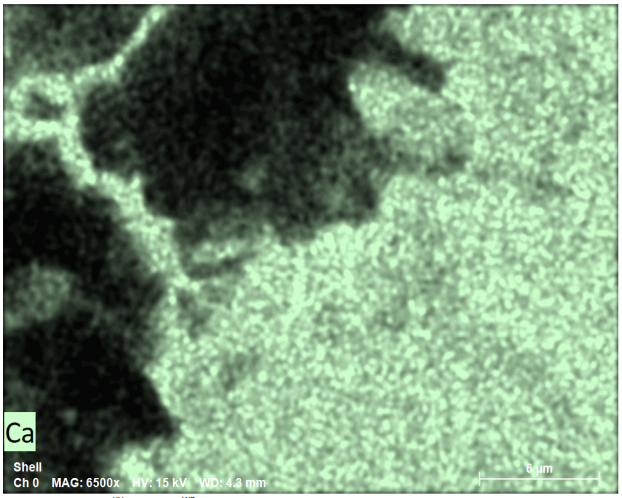

Date	Time	HV [kV]	Mag	WD [mm]
10/28/2019	4:01:03 PM	15.0 keV	6500x	4.3 mm

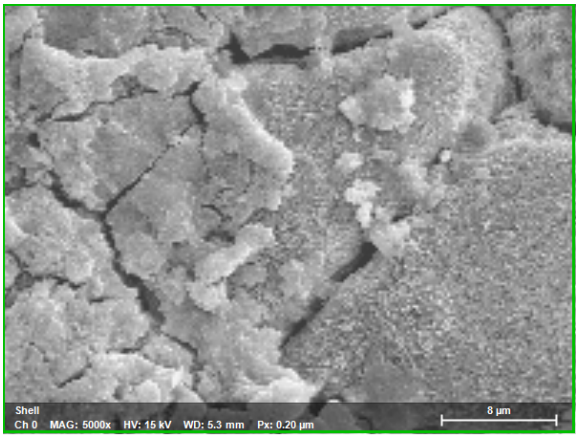

Name	Date	Time	HV [kV]	Mag	WD [mm]
Shell	10/28/2019	4:38:31 PM	15.0 keV	5000x	5.3 mm

Name	Date	Time	HV [kV]	Mag	WD [mm]
Shell	10/28/2019	4:38:57 PM	15.0 keV	5000x	5.3 mm